

Seasonal velocity variations over the entire Kuroshio path

Zhen-Long Zhang*

2021/05/17

The United School of Agricultural Sciences, Kagoshima University, 4-50-20 Shimoarata, Kagoshima 890-0056, JAPAN.

*Current affiliation: Faculty of Fisheries, Kagoshima University, Kagoshima, JAPAN.

ABSTRACT

This study investigated the seasonal velocity variations over the entire Kuroshio path at several depths based on different datasets. It was found that the seasonal velocity variations above ~500 m depth (upper layer) reaches a maximum in July while those below ~500 m depth (lower layer) reaches a maximum in winter over the broad area of the western boundary region. To clarify the essential driving mechanism of the seasonal velocity variations at different depths, numerical experiments were carried out using a regional model with a realistic bottom topography. The experiment results showed that the velocity variation in the upper layer is mainly caused by the local response to the wind stress just upon the Kuroshio, while the velocity variation in the lower layer is the remote response to the wind stress in the interior region of the North Pacific Ocean. Focusing on the seasonal velocity variations in the upper layer, an analytical model was also adopted to understand its dynamics. The findings showed that the shape of the velocity profile has a marked effect on the seasonal velocity variations of the Kuroshio in the upper layer: with a higher wavenumber on the west side of the velocity profile, the velocity of the Kuroshio is shown to increase under summer wind condition while decrease under autumn wind condition. These results provide a unified seasonal velocity variation feature over the entire Kuroshio path and a new insight into its mechanism.

Contents

1. Introduction	5
2. Data and methods	8
2.1. Data used for analysis	8
2.2. A coordinate that follows the direction of the Kuroshio	10
2.3. Hovmöller diagram	12
3. Results from data analysis	12
3.1. Seasonal velocity variations in the upper layer	12
3.2. Seasonal velocity variations in the lower layer	18
4. Discussions for the data analysis results	20
4.1. Driving mechanism for the upper-layer velocity variations	20
4.1.1. Numerical experiments with realistic bottom topography	20
4.1.2. Performance of the numerical model	25
4.1.3. Driving force for the seasonal upper-layer velocity variations	32
4.1.4. Hypothesis for the seasonal upper-layer velocity variations	36

4.2.	Driving mechanism for the lower-layer velocity variations	40
5.	Proving the hypothesis for the seasonal upper-layer velocity variations	42
5.1.	Numerical experiments with idealized bottom topography	43
5.1.1.	Checking the artificial signals	48
5.1.2.	Performance of the numerical model.....	49
5.2.	Analytical model used to explain the hypothesis.....	55
5.2.1.	Assumptions for the analytical model.....	57
5.2.2.	Explanations of the hypothesis based on an analytical solution	61
5.3.	Application of the hypothesis over the entire Kuroshio path	66
6.	Summary.....	66
7.	Acknowledgments	70
8.	Reference	70

1. Introduction

The Kuroshio, which is the western boundary current of the North Pacific subtropical gyre, originates from the region southeast of Luzon Island and flows northeastward along the continental slope passing through several geographically distinct regions: the Luzon Strait, the east of Taiwan, the East China Sea (hereafter, ECS) and the south of Japan (Figure 1). It contributes to the establishment of rich marine ecosystem in these areas and has great impacts on marine fisheries. For example, the eggs and larvae of numerous fish species are transported by the Kuroshio from their upstream spawning areas into the suitable nursery and fishing ground (Kasai et al. 2008). Not only the eggs and larvae, but also the nutrients can be transported by the Kuroshio so that the biological production is maintained to be high with the same level as in the high-latitude North Pacific (Guo et al. 2012). Investigating the temporal and spatial variations in the Kuroshio velocity is, therefore, crucial for our understanding of the variability in the fish resource.

For many years, numerous researchers have investigated seasonal variations in the Kuroshio transport in each separate region. Their historical efforts are briefly reviewed as follows. The Kuroshio transport reaches a maximum in October and a minimum in March for the region east of Luzon Island (Yaremchuk and Qu 2004); a maximum in July and a minimum in April to the east of Taiwan (Gilson and Roemmich 2002; Hsin et al. 2013); a maximum in summer and a minimum in autumn in the ECS (Ichikawa and Beardsley 1993; Kagimoto and Yamagata 1997; Andres et al. 2008); and for the region south of Japan, a maximum in summer and a minimum in winter (Sekine and Kutsuwada 1994) or a semiannual cycle with maxima in December and June-July (Isobe and Imawaki 2002; Zhu et al. 2017). Although these studies have revealed significant regional characteristics of the seasonal variations in the Kuroshio transport, a unified view of these variations over the entire Kuroshio path has yet to be established.

However, it is difficult to capture a unified seasonal overview of the entire Kuroshio path through an examination of transport variations alone. The first reason for this is that the estimated transport variations obtained from several repeat hydrographic sections across the Kuroshio (e.g., Ichikawa and Beardsley 1993; Imawaki 1997; Gilson and Roemmich 2002; Yaremchuk and Qu 2004) are too coarse to show the details of horizontal differences. The second reason is based on the need to separate the barotropic and baroclinic components in the transport, which is difficult to accomplish because it requires measurements through the entire water column, even though it is crucial to understanding the dynamics of seasonal transport variations. The last reason is related to mesoscale eddies, which have intraseasonal transport variations that are much larger in amplitude than the seasonal transport variations (Chang and Oey 2011). This means that a long time series is necessary to remove their transport components. To avoid these problems and to reveal the features of unified seasonal variations over the entire Kuroshio path, this study investigates seasonal velocity variations at different depths along the entire Kuroshio path using a satellite-altimetry-derived sea-surface geostrophic velocity dataset from a 19-year period and a three-dimensional (3D) assimilation velocity dataset below the sea surface for the same period.

On the other hand, the driving mechanism for the observed volume transport variations of the Kuroshio is still unclear, although it has been examined by many researchers in the areas of the ECS and south coast of Japan (Kubota et al. 1995; Kagimoto and Yamagata 1997; Sekine and Kutsuwada 1994; Sakamoto and Yamagata 1996; Isobe and Imawaki 2002). Their studies sought to clarify the following two problems. The first problem is that observed seasonal variations in the Kuroshio transport are much smaller in amplitude than those of nontopographic Sverdrup transport variations. The other is that the observed variations are approximately 180° out of phase with nontopographic Sverdrup transport variations. These two problems have been examined primarily from two dynamical aspects.

One aspect is the local dynamics in the western boundary region (hereafter, WBR). Using a linear barotropic model, Kubota et al. (1995) examined whether seasonal monsoon wind forcing reproduces the seasonal Kuroshio transport variations. They found that the phase of the annual cycle was well reproduced, although its amplitude was much smaller than that recorded in the observations. The cause of the seasonal transport variations in their model is the vorticity input over the continental slope by seasonal along-slope wind stress. The seasonal Florida Current transport variations are also characterized by a summer maximum and winter minimum (e.g., Schott et al. 1988). Czeschel et al. (2012) showed that the annual cycle of the Florida Current transport is predominantly related to coastal upwelling/downwelling caused by the wind stress field off the eastern coast of North America.

Other dynamics invoked to explain the seasonal Kuroshio transport variation are related to the effects of variable bottom topography, such as the continental slope (Sakamoto and Yamagata 1996), the Izu-Ogasawara Ridge (Greatbatch and Goulding 1989b, 1990; Sekine and Kutsuwada 1994; Isobe and Imawaki 2002), and a combination of both of these topographies (Kagimoto and Yamagata 1997). For example, Sakamoto and Yamagata (1996) examined the continental slope effect for the Joint Effect of Baroclinicity and Relief (JEBAR), whereas Isobe and Imawaki (2002) focused on the blocking effect of the Izu-Ogasawara Ridge on the westward-propagating barotropic Rossby waves. However, neither study clearly explained the phase discrepancy in the seasonal variations that exists between the observed transports and the nontopographic Sverdrup volume transports, even though they did show a volume transport reduction. On the other hand, Kagimoto and Yamagata (1997) succeeded in reproducing seasonal variations in the Kuroshio volume transport both in amplitude and phase using a numerical model with a realistic bottom topography. They related the mechanism of seasonal variations to the JEBAR based on the vorticity balance for the vertically integrated flow but did not investigate the concrete processes involved

in the JEBAR. The bottom topography may certainly play an important role in seasonal volume transport variations of the Kuroshio, but the definitive mechanism is still unclear, especially its phase with a maximum in summer and a minimum in winter.

As mentioned above, the definitive mechanism explaining the summer maximum of the volume transport variation is still unclear. Especially, the roles of the local dynamics in the WBR and the Sverdrup dynamics in the interior region as the driving mechanisms for the seasonal Kuroshio transport variations are still subject to debate. Therefore, numerical experiments were conducted in this study to clarify which dynamics are essential for seasonal transport variations. Analytical model was also used to understand the dynamics for the seasonal variations. It should be noted that this study focused on the seasonal velocity variations at different depths along the entire Kuroshio path instead of the volume transport. This is because this study seeks to understand individual processes relating to volume transport.

2. Data and methods

2.1. Data used for analysis

Two kinds of geostrophic velocity data were analyzed in this study. One dataset is the Gridded Sea Level Anomalies and Absolute Dynamic Topography Heights and Currents in the Delayed-TimeTwo-Sat Series product from the Copernicus Marine Environmental Monitoring Service (CMEMS). This dataset, which has a spatial interval of $1/4^\circ$ (latitude) \times $1/4^\circ$ (longitude), has been produced since January 1993 and was used for showing the seasonal velocity variation at the sea surface in this study. Another dataset, which is a 3D assimilation data product named the Multivariate Ocean Variational Estimation system- western North Pacific (MOVE-WNP), was used to investigate seasonal velocity variations under the sea surface. This dataset was developed by the Meteorological Research Institute of the Japan Meteorological Agency (MRI/JMA) (Usui

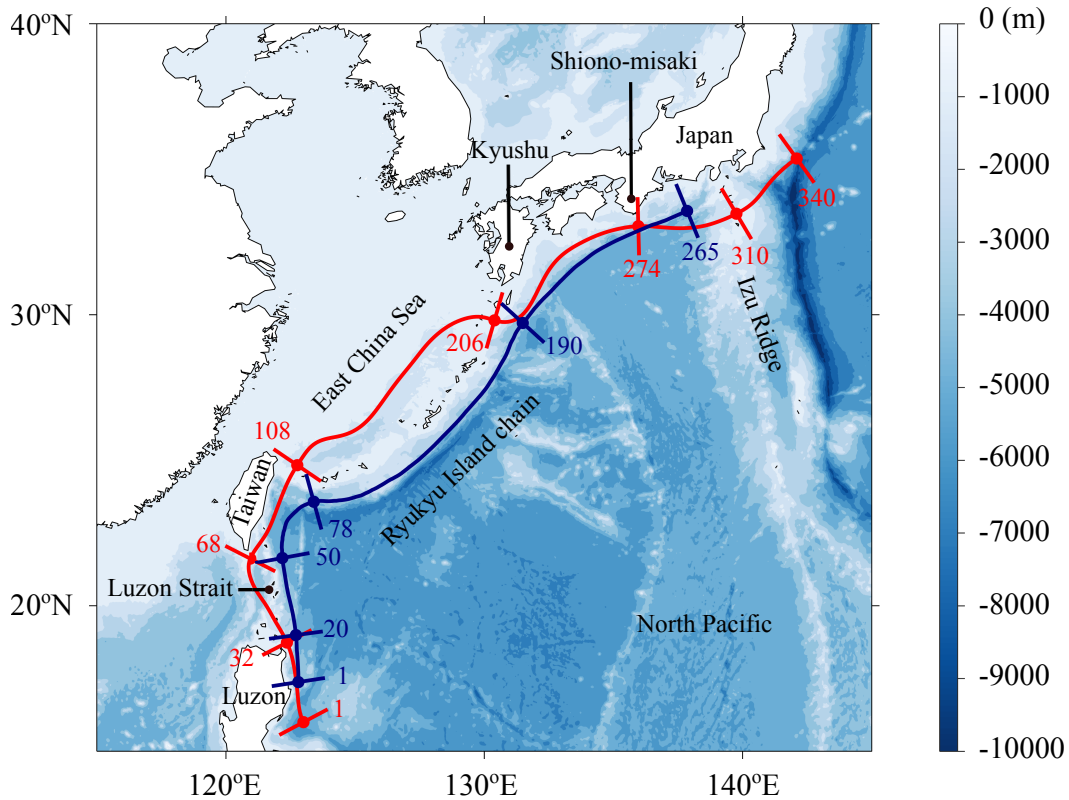


FIG. 1. The study areas for the investigation of seasonal velocity variations along the current path of the Kuroshio. The shaded blue color indicates the bottom topography. The red line denotes the upper layer (0-500 m depth) Kuroshio path, which is based on the annual mean velocity field derived from CMEMS altimeter data. The blue line shows the lower layer (> 500 m depth) Kuroshio path, which corresponds to the 3500 m isobath. To estimate along-stream velocity components, the cross sections (220 km in length) perpendicular to the Kuroshio path are formed with a 10 km spatial interval along the Kuroshio path. The key cross sections that separate the individual regions are shown with the cross section number. Table 1 summarizes all the cross section numbers for identifying the individual regions along the Kuroshio path, based on different datasets.

et al. 2013) and is also a daily product with a spatial interval of $1/10^\circ$ (latitude) \times $1/10^\circ$ (longitude) and 54 levels in the vertical direction. For consistency, all of the two datasets were examined for the same period from 1993 to 2011 and same coverage over the entire Kuroshio path from the east

of Luzon Island to south coast of Japan (120° E to 160° W, 15° N to 45° N). The climatological monthly means for 19 years from 1993 to 2011 were calculated for both of the two datasets. Climatological monthly anomalies fields extracted from the annual means were analyzed and will simply be called the “monthly anomalies” hereafter.

2.2. A coordinate that follows the direction of the Kuroshio

To attain a unified view of seasonal Kuroshio velocity variations at different depths, along-stream coordinates with a series of cross sections that almost perpendicularly across the Kuroshio for the upper- and lower- layers were adopted in this study. The upper layer is defined as the layer shallower than 500 m, while the lower layer is defined as the layer deeper than 500 m.

For the upper layer along-stream coordinate (red line in Figure 1), the following steps were proceed: 1) Set a start point at the location 123° E, 16° N; 2) Calculate an annual mean velocity vector by averaging in the 50 km radius around the start point; 3) Draw a cross section perpendicular to the direction of the annual mean velocity vector, which consists of 23 points (10 km interval) for a length of 220 km; 4) Move the start point 10 km downstream; and 5) repeat steps 1-4. The normal velocity components are thus estimated at 23 points for each of the cross sections. The normal velocity components are thus estimated at 23 points for each of the cross sections. Since the annual mean velocity vectors differ with datasets, cross sections should be constructed based on different datasets. Table 1 summarizes the cross sections for identifying the individual regions based on different datasets, including the CMEMS altimetry data, the MOVE-WNP reanalysis data and numerical experiment outputs.

The deep water of the Kuroshio in the ECS is isolated from the western North Pacific by the Ryukyu Island chain (Figure 1). This topographic feature is responsible for the Ryukyu Current system on the eastern slope of the Ryukyu Island chain (e.g., Zhu et al. 2003; Ichikawa et al.

TABLE 1. Cross section numbers for identifying the individual regions along the Kuroshio path, based on different datasets.

	East of Luzon Island	Luzon Strait	East of Taiwan	East China Sea	South of Japan	Related figures
Altimeter data	1-32	32-68	68-108	108-206	206-340	1,3a
Reanalysis data	1-32	32-70	70-110	110-210	210-340	3b,4
Model outputs						
Exp-1	1-20	20-48	48-87	87-205	205-340	9a,11a,13a
Exp-2	1-20	20-127	127-165	165-275	275-340	9b,11c
Exp-3	1-20	20-48	48-87	87-205	205-265	9c,13b
Exp-4	1-20	20-48	48-87	87-205	205-340	9d,13c

2004), which is characterized by a subsurface current core at 500-1000 m depths off the northern Ryukyu Islands but a nearly barotropic structure off the southern Ryukyu Island (Nakamura et al. 2007). Thus, it is reasonable to regard the eastern slope of the Ryukyu Island chain as a route of the deeper Kuroshio flow. Since the Ryukyu Current system flows along the isobaths of the continental slope, its direction is considered to be the direction of the isobath. Here, in addition to the upper layer along-stream coordinate, the 3500 m isobath was defined as the lower layer along-stream coordinate (blue line in Figure 1).

2.3. Hovmöller diagram

The seasonal velocity variations at different depths were shown through the Hovmöller diagrams of monthly velocity anomalies along the stream coordinate in this study. The normal velocity components were averaged on each cross section. By this way, the changes in the magnitude of velocity, i. e., the current speed variation, can be shown more clearly. This is because the changes in the current axis (location of the maximum normal component at each cross section) are much reduced by the averaging. Notice that this method is suitable only when the current axis variation is small when comparing to the width of the cross section (220 km in the case of this study). For the area where large current axis variation occurs, e. g., the Kuroshio large meander off the south coast of Japan (Kawabe 1995), this method needs to be used carefully. It was confirmed that the current path of the Kuroshio was stable and was predominant by the nearshore nonlarge-meander path (Kawabe 1995) in the period from 1993 to 2011. Therefore, the Hovmöller diagrams takes little influence from the current axis variation and mainly indicates the changes in the current speed.

3. Results from data analysis

3.1. Seasonal velocity variations in the upper layer

To capture an overview for the seasonal surface velocity variations over the entire Kuroshio path, monthly kinetic energy anomalies are shown in Figure 2. It can be seen that the kinetic energy anomalies tend to be positive over the entire Kuroshio path during the period from April to September and negative during all the other months. More specifically, in July and August, positive anomalies occupy the whole Kuroshio width and cover the entire Kuroshio path. Except for in July and August, paired positive and negative anomalies across the entire Kuroshio width tend to appear at some locations along the Kuroshio path. The two different patterns of the horizontal distribution

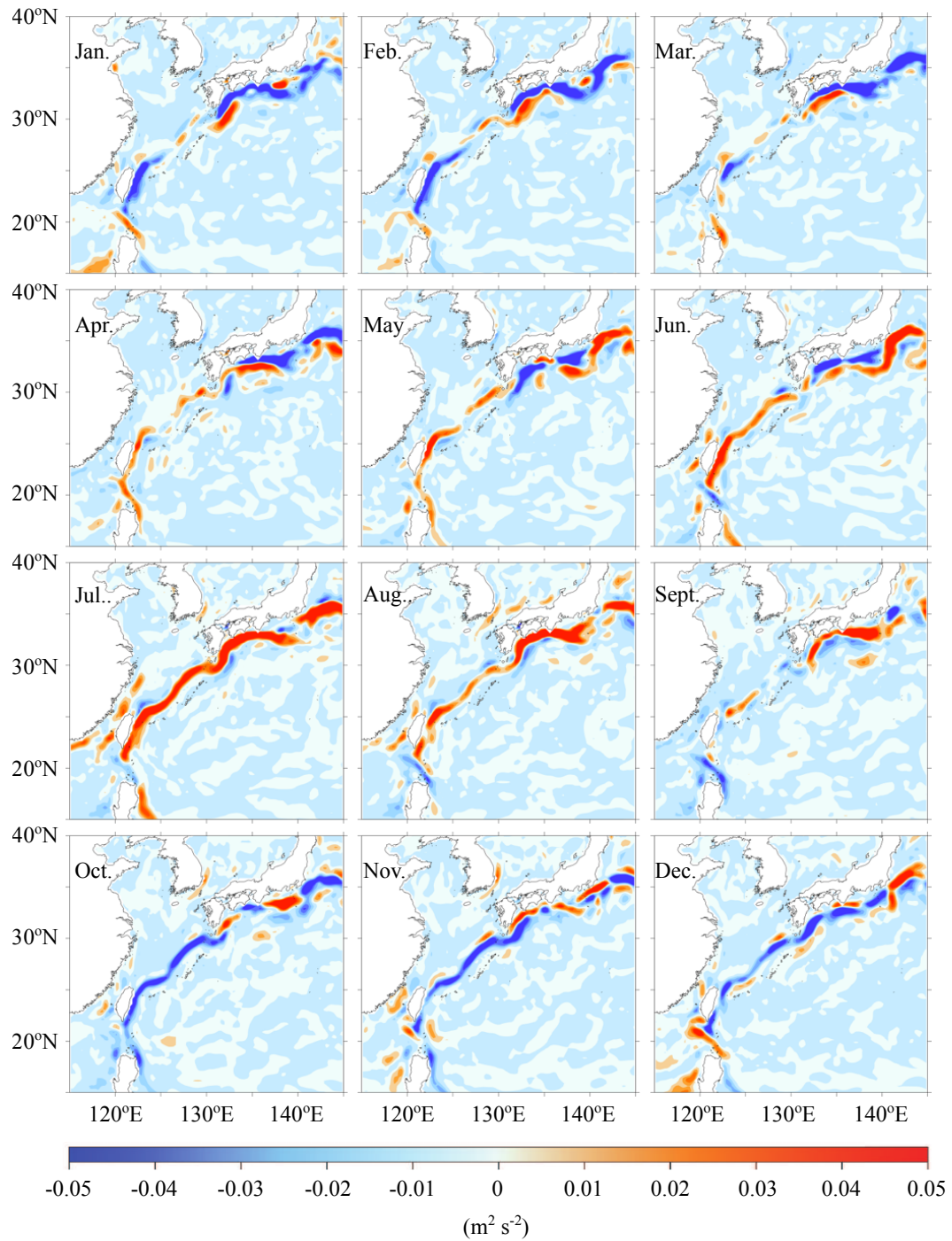


FIG. 2. Horizontal distributions of the monthly surface kinetic energy anomalies from the annual means covering the period from 1993 to 2011 based on CMEMS altimeter data. The red (blue) color indicates positive (negative) anomalies.

imply two kind of seasonal variations occurring in the velocity field, i. e., current axis and current speed variations. The current variation introduces positive anomalies on one side of the Kuroshio while negative anomalies on the other side of the Kuroshio, therefore, results in paired positive and negative anomalies distribution in Figure 2. On the other hand, the current speed variation introduces single positive or negative anomalies across the width of the Kuroshio so that it only results in a single positive or negative anomalies distribution in Figure 2. The different types of horizontal anomaly distributions in Figure 2 indicate that the two types of seasonal variations dominate the variations in the velocity field of the Kuroshio for different periods. It is, therefore, necessary to suppress the changes in the current axis, which is to average the normal velocity components on each cross section in this study.

To focus on the current speed variation over the entire Kuroshio path, the seasonal variations in the velocity field are represented by Hovmöller diagrams. It can be clearly seen that (Figure 3a) the maximum anomalies appear in summer (June, July, August) for the most regions over the entire Kuroshio path (i.e., east of Luzon Island, east of Taiwan, the East China Sea, south coast of Japan), except in the Luzon Strait where the maximum anomalies appear in later winter (December) and early spring (March and April). Propagation signals are found in the area from Cape Shinonomisaki (denoted by CSM in Figure 3a) to Izu Ridge (IR in Figure 3a) where the maximum anomalies shift from July to August.

As reviewed in Section 1, numerous studies have reported that seasonal Kuroshio transport variations are characterized by a maximum in summer (Ichikawa and Beardsley 1993; Sekine and Kutsuwada 1994; Kagimoto and Yamagata 1997; Gilson and Roemmich 2002; Isobe and Imawaki 2002; Andres et al. 2008; Hsin et al. 2013; Zhu et al. 2017). Therefore, based on the long-term averaged time series, the seasonal variations with summer observed in this study are rarely considered to be wrong even the seasonal variations are modified by mesoscale eddies (e.g.,

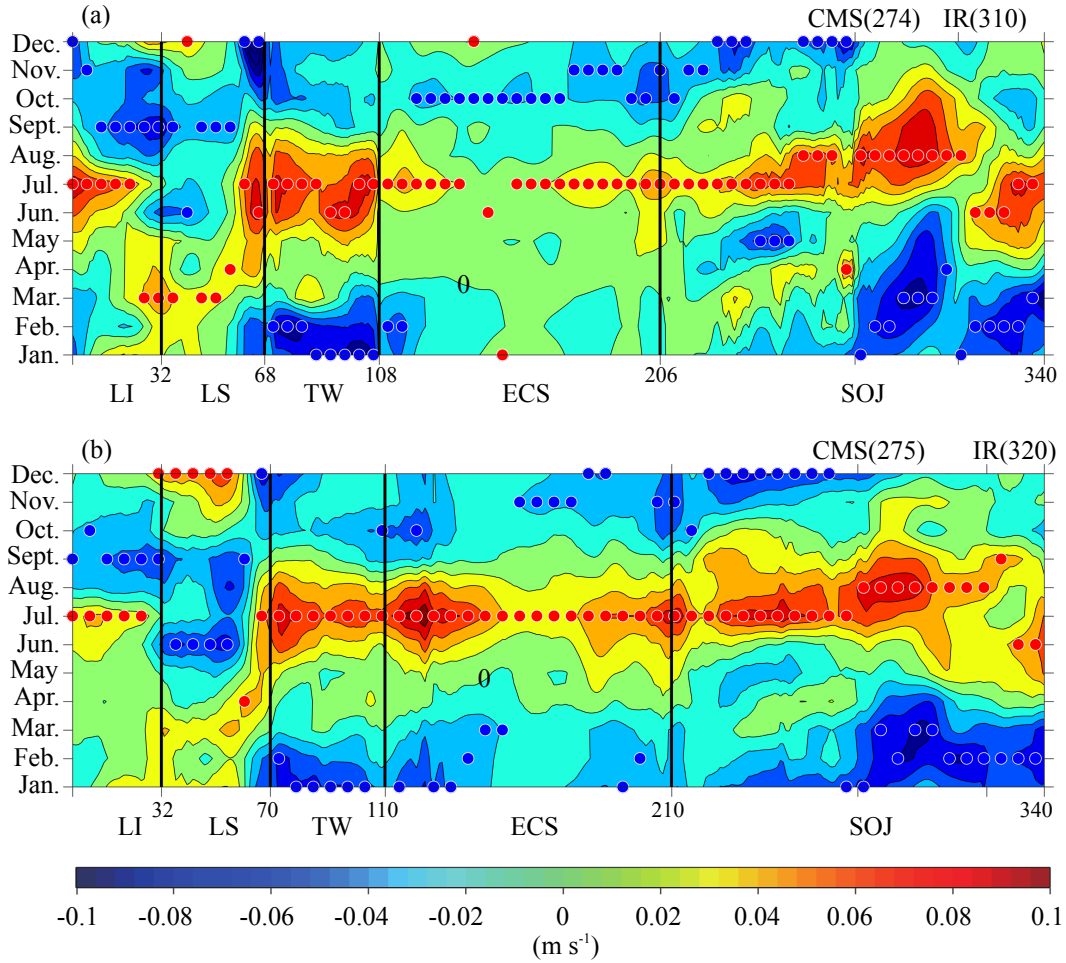


FIG. 3. Hovmöller diagram of the monthly surface velocity anomalies from the annual means covering the period from 1993 to 2011 over the entire Kuroshio path based on the (a) CMEMS altimeter data (see Figure 1 for the upper layer Kuroshio path) and (b) MOVE-WNP reanalysis data (the path is not shown). The red (blue) dot at each location indicates a maximum (minimum) anomaly for the year. The horizontal axis indicates the cross section number, whose increment by 1 corresponds to the 10 km distance along the Kuroshio path. The vertical black lines are drawn to separate the individual regions. LI: east of Luzon Island; LS: Luzon Strait; TW: east of Taiwan; ECS: East China Sea; SOJ: south coast of Japan; CSM: Cape Shionomisaki; IR: Izu Ridge. The contour interval is 0.02 m s^{-1} .

Chang and Oey 2011). In addition to the previous studies, results in this paper indicate that the July maximum is not a separate regional feature but is instead a coherent feature spanning most areas over the entire Kuroshio path. Minimum anomalies (Fig. 3a) tend to appear in two seasons: autumn (September to November) and winter (December to February). The autumn minimum dominates a broad area from the east of Luzon Island to the ECS, whereas the winter minimum appears off the east coast of Taiwan and in the areas from the Tokara Strait to Cape Shinonomisaki. From Cape Shinonomisaki to the Izu Ridge, both the maximum (August) and minimum (February to April) anomalies tend to propagate downstream.

Similar seasonal features can also be obtained in MOVE-WNP reanalysis dataset. In Figure 3b, it can be seen that the sea surface current speed variations correspond closely to those in Figure 3a. Specifically, the appearance of the maximum and minimum anomalies over the entire Kuroshio path, i.e., summer maximum and autumn (October to November) or winter (January to February) minimum. Analysis on the similarity between Figure 3a and Figure 3b shows that the correlation coefficient (r) for the two figures exceeds the 95% confidence level (0.58) in all areas ($r > 0.80$) except for Luzon Strait ($r = 0.33$). It is, therefore, considered that the seasonal feature derived in this study does not rely on particular dataset but is a general feature that can be observed in different datasets.

Using the same cross sections as in Figure 3b, the current speed variations below the sea surface are investigated. The features of the seasonal velocity variations at 200 m depth (Figure 4a) have a pattern that is similar to that at the sea surface (Figure 3b): the correlation coefficient is significant at the 95% confidence level in the areas from the east of Taiwan to the south of Japan ($r > 0.71$), while not significant east of Luzon Island ($r = 0.33$) and in the Luzon Strait ($r = -0.57$). Similar seasonal features of the current speed variation can also be found at 400 m depth, except that the amplitudes of the current speed variation decrease comparing to those at a shallower depth. As the

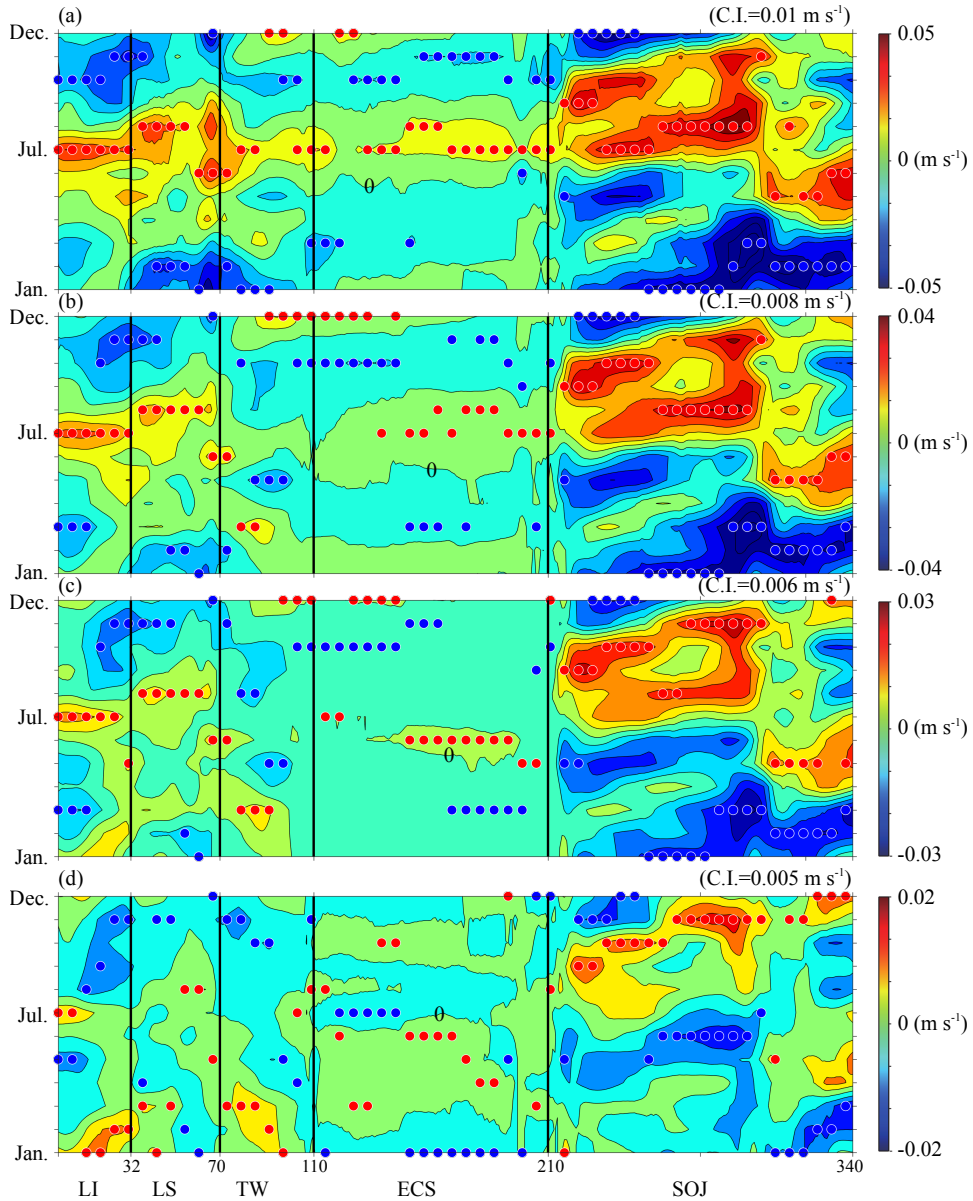


FIG. 4. Hovmöller diagram of the monthly velocity anomalies from annual means covering the period from 1993 to 2011 based on the MOVE-WNP reanalysis data at different depths: (a) 200 m; (b) 400 m; (c) 600 m; (d) 1000 m. The color bar range and the contour interval are different from each plot for a better display. The red (blue) dot at each location indicates a maximum (minimum) anomaly for the year. The horizontal axis indicates the cross section number, whose increment by 1 corresponds to the 10 km distance along the Kuroshio path. The vertical black lines are drawn to separate the individual regions. LI: east of Luzon Island; LS: Luzon Strait; TW: east of Taiwan; ECS: East China Sea; SOJ: south coast of Japan.

depth increases to more than 400 m, the periods with the maximum anomalies appear in months other than July. Specifically, the maximum anomalies appear from January to March at a depth of 1000 m (Figure 4d) in the area from the east of Luzon Island to the east of Taiwan, while they appear from September to November at 600-1000 m depths (Figures 4c-d) in the area off the south coast of Japan. These results indicate that the seasonal feature of the current speed variations is not the same over the entire water column. Therefore, the driving mechanism should be considered separately for the current speed variations at different depth. Regarding to the similarity of the seasonal feature upon 600 m, this study defined the upper layer as the layer shallower than 500 m while the lower layer as the layer deeper than 500 m. In the next subsection, the seasonal feature for the lower layer current speed variations is discussed.

3.2. Seasonal velocity variations in the lower layer

Since the velocity in the lower layer is significantly smaller than that near the sea surface, it is better to show the seasonal variations with depth-averaged velocity rather than velocity at different depths. Figure 5a shows the seasonal feature over the entire Kuroshio path in the lower layer. Here, instead of the depth-averaged velocity, the volume transport is used here, because it is convenient to discuss the dynamics in the lower layer in Section 5b. It shows that most of the maximum anomalies are present during winter (December, January, and February) in the broad area from the east of Luzon Island to the east of the Ryukyu Island chain. On the other hand, most of the minimum anomalies appear during autumn (from September to November) over the whole region, even though some scattered minimum anomalies appear around April. The similar seasonal features are also found for the total volume transport variations (Figure 5b), which are calculated by integrating the velocity from the sea surface to the bottom, except that the amplitudes of the seasonal variation over the entire along-stream coordinate increase by a mean value of approximately 4 Sv (1 Sv =

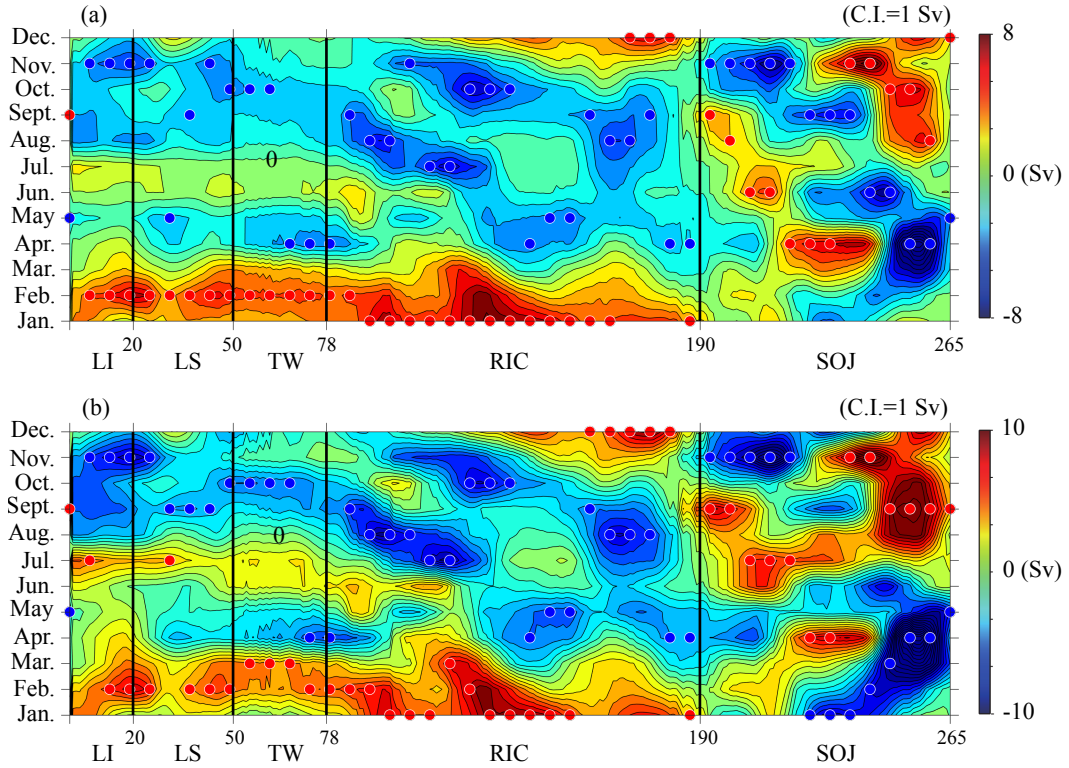


FIG. 5. Hovmöller diagram of the monthly volume transport anomalies, obtained at each cross section (see Figure 1 for the lower layer Kuroshio path) by integrating the velocities (MOVE-WNP reanalysis data) from (a) the 500 m depth to the bottom and (b) the sea surface to the bottom. The red (blue) dot at each location indicates a maximum (minimum) anomaly. The horizontal axis indicates the cross section number, whose increment by 1 corresponds to the 10 km distance along the Kuroshio path. The vertical black lines are drawn to separate the individual regions. LI: east of Luzon Island; LS: east of Luzon Strait; TW: east of Taiwan; RIC: east of Ryukyu Island chain; SOJ: south coast of Japan.

$10^6 \text{ m}^3 \text{ s}^{-1}$). These seasonal features in the lower and over the entire water column are in contrast to those in the upper layer, especially for the appearance of the maximum anomalies. Therefore, the driving mechanism used for explaining the seasonal variations in the lower layer could not be applied for the seasonal variations in the upper layer so that they should be considered separately as pointed in the previous subsection.

4. Discussions for the data analysis results

4.1. *Driving mechanism for the upper-layer velocity variations*

4.1.1. *Numerical experiments with realistic bottom topography*

The primary purpose of numerical experiments is to clarify which dynamics are the essential, local dynamics within the WBR or the Sverdrup dynamics in the interior region, as the driving mechanisms for seasonal velocity variations at different depths over the entire Kuroshio path. For this purpose, the Princeton Ocean Model (POM) (Blumberg and Mellor 1987) is adopted with a configuration for model domain to cover the western North Pacific (110° E to 170° E, 5° N to 55° N). The bottom topography in the model domain is based on the 1arc-minute global relief model (ETOPO1), which is provided by the National Center for Environmental Information (NCEI) (Amante and Eakins 2009). The maximum depth of the modeled ocean is set at 5000 m and the minimum depth is set at 10 m. The modeled bottom topography is smoothed by using a slope parameter (Mellor et al. 1998), which is less than 0.2 over the model domain. The model ocean is integrated using several types of annual-cycle wind stress forcing with different spatial distributions for different purposes. The wind stress data are the surface boundary condition used for the OGCM For the Earth Simulator (OFES) (Masumoto et al. 2004; Sasaki et al. 2004), which is a global model (resolution: $1/10^{\circ} \times 1/10^{\circ}$; period: January 1993 to December 2011) forced by climatological monthly mean wind stresses from the National Centers for Environmental Prediction and the National Center for Atmospheric Research (NCEP/NCAR) (Kalnay et al. 1996). Other boundary conditions are, however, fixed to be annual-mean states. Such numerical experiments are designed as follows: The simulation for Experiment 1 (Exp-1) is a control run, which is forced by wind stresses with annual cycle variations (Figure 6) over the whole model domain to reproduce the seasonal velocity variations over the entire Kuroshio path. One overall feature of the seasonal

variations is that the wind stress in the WBR is dominated by the East Asian monsoon, thereby resulting in generally northward wind stresses in summer and southward to southwestward wind stresses in winter over the WBR from east of Luzon Island to the south of Japan (Figure 6). Exp-2, in which wind stresses over the entire WBR are removed (Figure 7b), is performed to verify the effect of wind stress over the WBR. To check regional effects of the wind stress within the WBR, the wind stress over the WBR is partially removed in the following experiments (Exp-3 and Exp-4): Exp-3 is a scenario with no wind stress in the ECS (Figure 7c), and Exp-4 is a scenario with no wind stress near the north of Taiwan (Figure 7d).

The model is configured as follows. The horizontal grid is a variable spherical grid that consists of 341 cells both in the longitudinal and latitudinal directions. The grid in the area ranging from 120-140° E to 15-40° N has a spatial interval of 1/8° both in the longitudinal and latitudinal directions. Outside this area, the spatial interval changes gradually to 1/2° in the longitudinal direction and to 1/4° in the latitudinal direction. The vertical grid has 21 sigma levels. The lateral boundaries are closed at the western and northern sides and open at the eastern and southern sides of the model domain. The Sommerfeld radiation condition is applied for the normal external and internal velocity components on the southern open boundary, while only the internal velocity on the eastern open boundary is used. The normal component of external velocity on the eastern open boundary is given by an inflow boundary condition that is specified based on the nontopographic Sverdrup transport value obtained by zonal integration of the climatology annual mean wind stress curl from the eastern boundary to 170° E. For this calculation, we use the monthly mean wind stress data from NCEP/NCAR reanalysis dataset, which are averaged from 1993 to 2011. The tangential velocity components on the eastern and southern open boundaries are set to zero.

For temperature and salinity boundary conditions, the annual climatological mean data with a spatial interval of one degree from the World Ocean Atlas 2001 (WOA01) (Conkright et al. 2002)

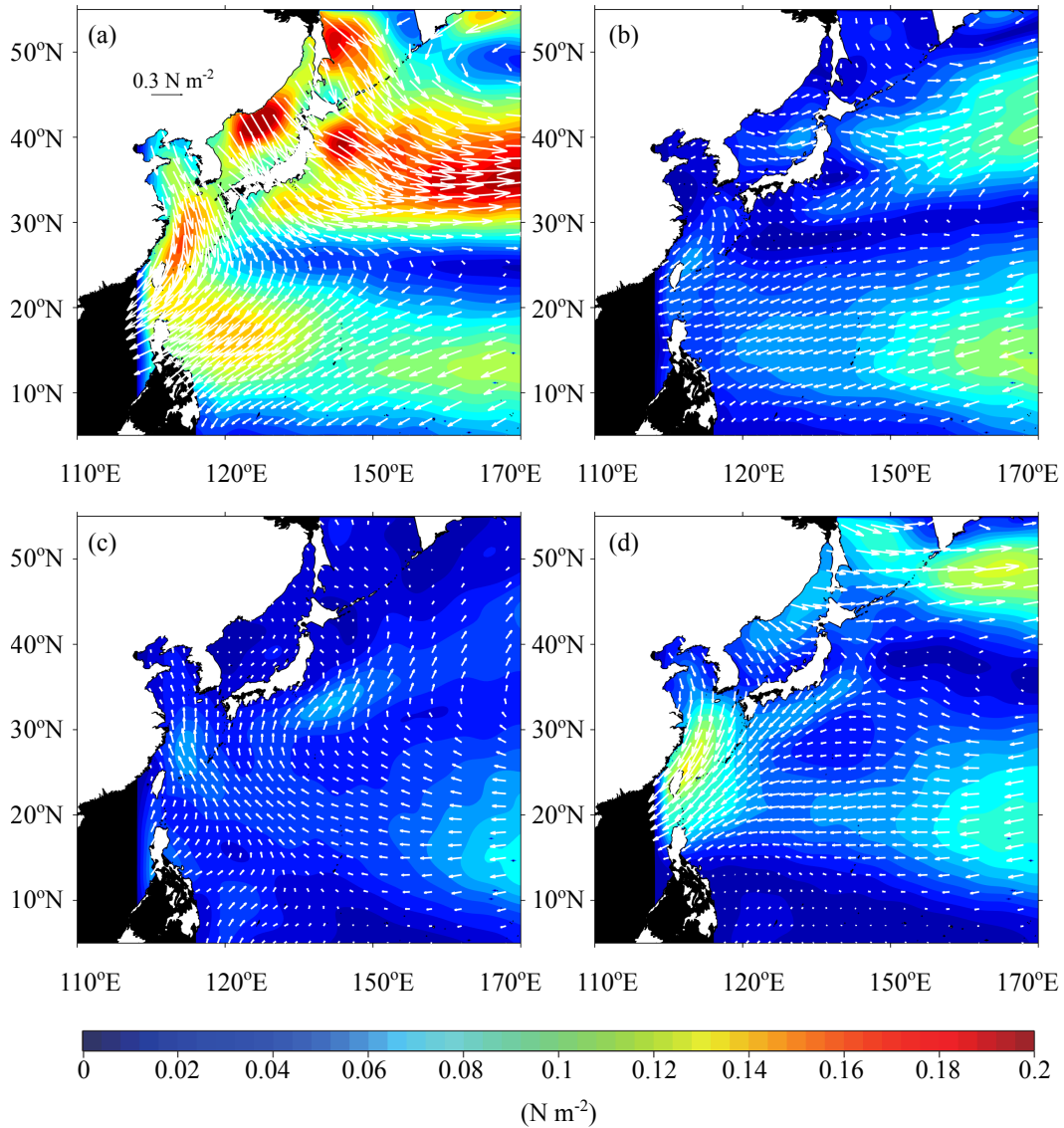


FIG. 6. Horizontal distribution of the monthly mean wind stresses (magnitudes shown in shaded colors) based on the NCEP/NCAR data for the period from 1993 to 2011. (a) January; (b) April; (c) July; (d) October. The areas without wind forcing are shaded in black. These wind stress fields are used to drive the control run.

are used. An upstream advection condition is applied for temperature and salinity on the eastern and southern open boundaries. To suppress internal Kelvin wave propagation along the southern boundary, the temperature and salinity are relaxed to the annual means within a Rayleigh sponge layer (450 km wide) around the southern open boundary. The sea surface temperature and salinity

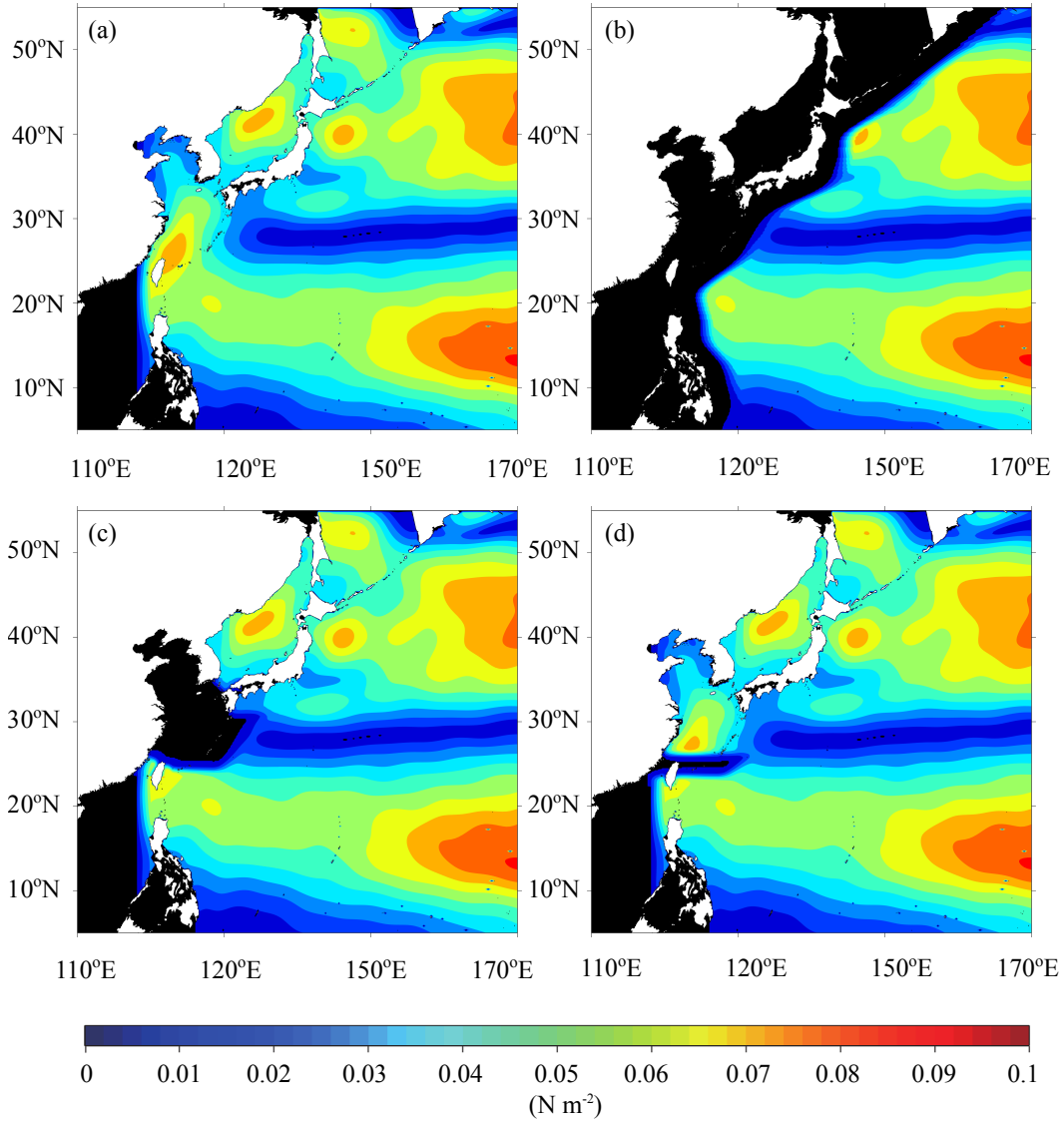


FIG. 7. Horizontal distributions of the mean annual wind stress magnitudes based on NCEP/NCAR data for the period from 1993 to 2011. (a) Exp-1; (b) Exp-2; (c) Exp-3; (d) Exp-4. The areas without wind forcing are shaded in black.

are relaxed to the annual means by the Haney-type formulation (Haney 1971) with an air-sea interaction coefficient of approximately 0.3 m d^{-1} .

The initial condition of the numerical model is defined by the annual climatological mean temperature and salinity data (WOA01). The model ocean is integrated over 20 years for each

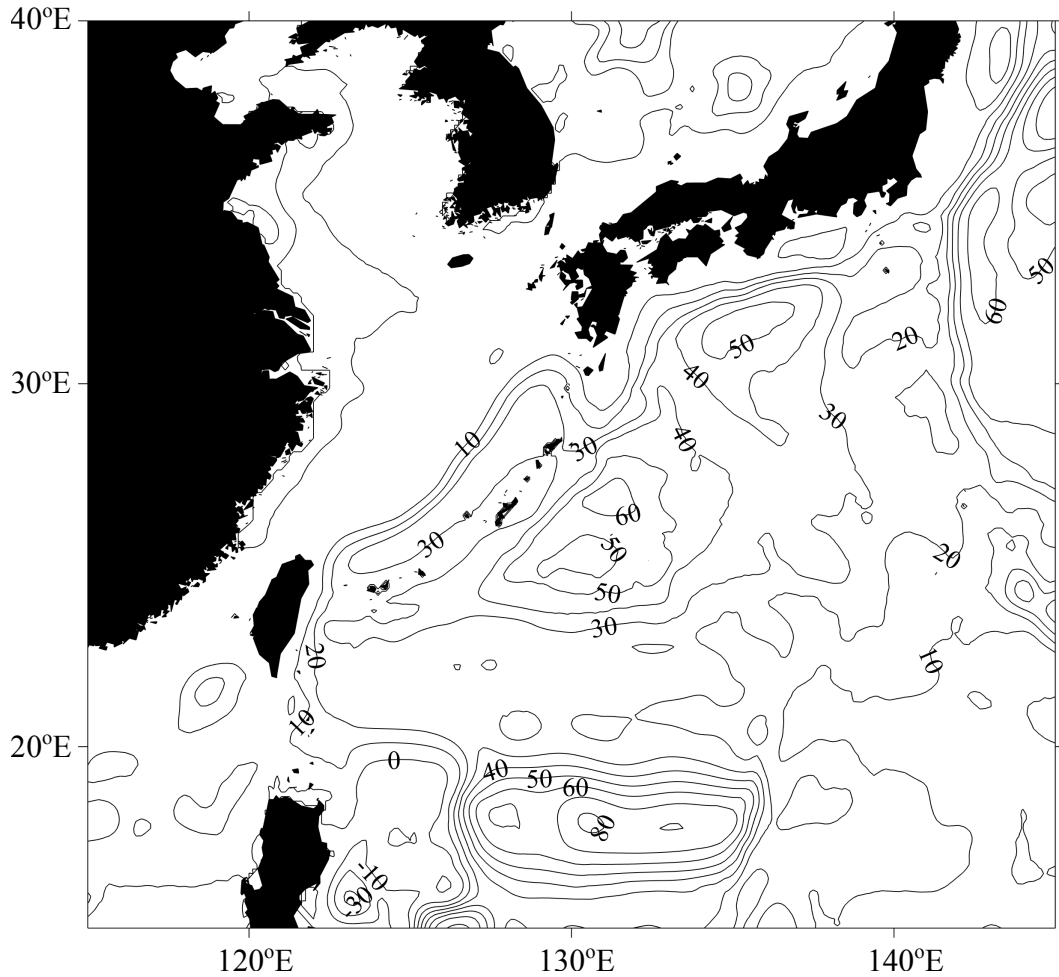


FIG. 8. Horizontal distribution of the stream function (5-year averaged) from Exp-1. The contour interval is 10 Sv ($1 \text{ Sv} = 10^6 \text{ m}^3 \text{ s}^{-1}$).

experiment. The time steps for the external and internal modes are set to 12 s and 240 s, respectively. Annual cycle variations in the velocity field are analyzed using monthly mean values averaged over the period from the 16th to the 20th year. The Smagorinsky-type formulation, with a nondimensional constant of 0.2, is used to calculate the horizontal kinematic viscosity (A_m) and the horizontal temperature/salinity diffusivity (A_h). The value of A_h/A_m is set to 0.2.

4.1.2. Performance of the numerical model

In this subsection, the reliability of the model results are validated. For this purpose, Kuroshio current structures for Exp-1 with those structures revealed by the observation and reanalysis data are compared. The comparisons are first performed for the annual mean states and then for the seasonal variations.

For the annual mean states, the barotropic structures for Exp-1 based on the annual mean depth-integrated stream function (Figure 8), which is calculated as the average over years 16 to 20, are evaluated. The volume transport of the Kuroshio reaches a maximum value of approximately 10 Sv around the Luzon Strait, 20 Sv off the east coast of Taiwan, 30 Sv in the ECS, and 50 Sv off the south coast of Japan. These values closely correspond to the observed Kuroshio volume transports: 6 ± 3 Sv around the Luzon Strait (Tian et al. 2006), ~ 21.5 Sv off the east coast of Taiwan (Johns et al. 2001), ~ 27 Sv in the ECS (Ichikawa and Beardsley 1993), and ~ 57 Sv off the south coast of Japan, a part of which is associated with a stationary local anticyclonic recirculation gyre (Imawaki et al. 2001).

A further look at Figure 8 shows a northward current with the transport of ~ 20 Sv along the eastern slope of the Izu-Ogasawara Ridge. This is regarded as a barotropic component of the western boundary current trapped on the eastern slope of the Izu-Ogasawara Ridge. A similar northward current has also been reproduced by other numerical simulations. For example, using a POM with a realistic bottom topography, Kagimoto and Yamagata (1997) (see Figure 5 in their paper) showed a stream function pattern that was similar to the one obtained in this study. However, the northward current of this study seems to be slightly stronger on the eastern slope of the Izu-Ogasawara Ridge because the Kuroshio in our model takes a stationary nearshore non-large-meander path south of Japan (Kawabe 1995). Another noticeable feature of the barotropic component is that the simulated Kuroshio overshoots northward along the east coast of Japan, merging with the northward current component along the eastern slope of the Izu-Ogasawara Ridge.

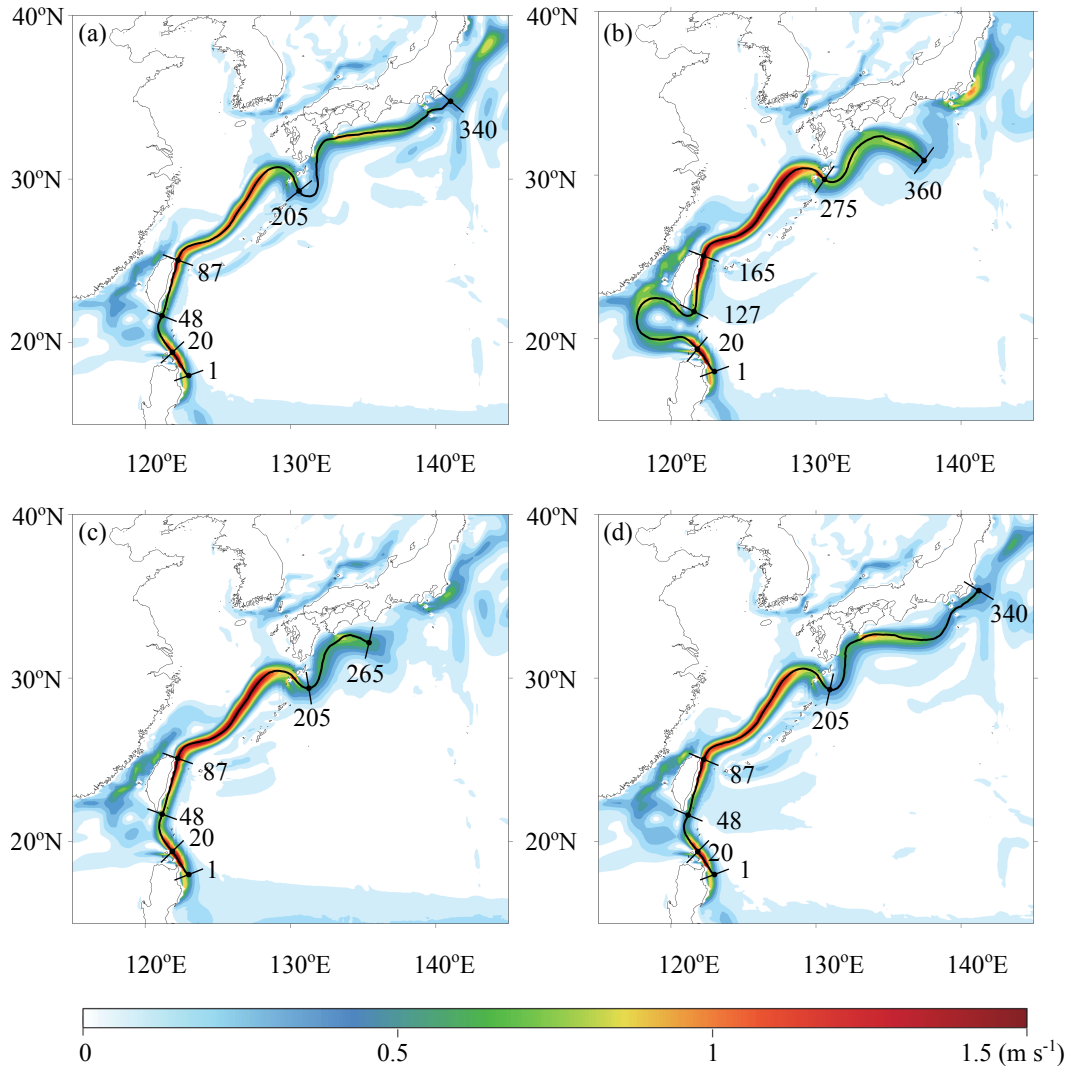


FIG. 9. Horizontal distributions of the annual mean absolute sea surface velocities from (a) Exp-1, (b) Exp-2, (c) Exp-3 and (d) Exp-4. The black line in each plot is the upper layer Kuroshio path, which is defined to each experiment. The cross section numbers for identifying the individual regions are denoted in each plot (see Table 1 for their correspondences).

The annual mean surface current field for Exp-1 (Figure 9a) shows that the current path of the Kuroshio at the sea surface is well reproduced, except for the fact that it overshoots northward along the east coast of Japan. The absolute surface velocity magnitude for Exp-1 is larger over the upstream Kuroshio region to the Tokara Strait than in its downstream region. In a comparison with

the annual mean surface velocity field obtained from the CEMES altimeter data, it is noticed that the simulated velocity magnitude is larger than that observed for the upstream region of the Tokara Strait, especially for the ECS. Comparing the model output with the MOVE-WNP reanalysis data, it was confirmed that the density stratification and the related horizontal density gradient for the upper-layer Kuroshio in the ECS are somewhat stronger in our model output than in the MOVE-WNP reanalysis data (figure not shown). This is a direct cause of the Kuroshio surface velocity intensification in our model, according to the thermal wind relation. The mechanism generating the stronger stratification is uncertain in this study, but it may be related to the surface and lateral boundary conditions in the model, in which temperatures are prescribed to be annual mean values.

For the seasonal variations, the monthly kinetic energy anomaly fields at the sea surface for Exp-1 (Figure 10) with those derived from the CEMES altimeter data (Figure 2) are compared. Both fields are quite consistent in terms of the overall seasonal variation structure. More specifically, the Kuroshio kinetic energy anomalies are positive during the period from April to September and negative during the other months. A noticeable feature in Figure 10 is the remarkable development of a loop current and a consequent eddy shedding during the period from February to May. This seasonal feature is consistent with obtained observational evidence that the loop current develops in winter (e.g., Wu and Hsin 2012), although the loop current for Exp-1 tends to be overemphasized.

Based on the Hovmöller diagram of the surface velocity anomalies (Figure 11a) along the upper layer Kuroshio path (black line in Figure 9a), the maximum and minimum anomaly distributions for Exp-1 are consistent with those derived from the CEMES altimeter data (Figure 3a) for the broad region from the east of Taiwan to the south coast of Japan (statistically significant at the 95% confidence level with $r > 0.65$ for area-averaged time series), except for the fact that the downstream propagation tendency of positive and negative anomalies is present in the ECS. However, Figure 11a shows that seasonal variations for Exp-1 are almost 180° out of phase with those derived

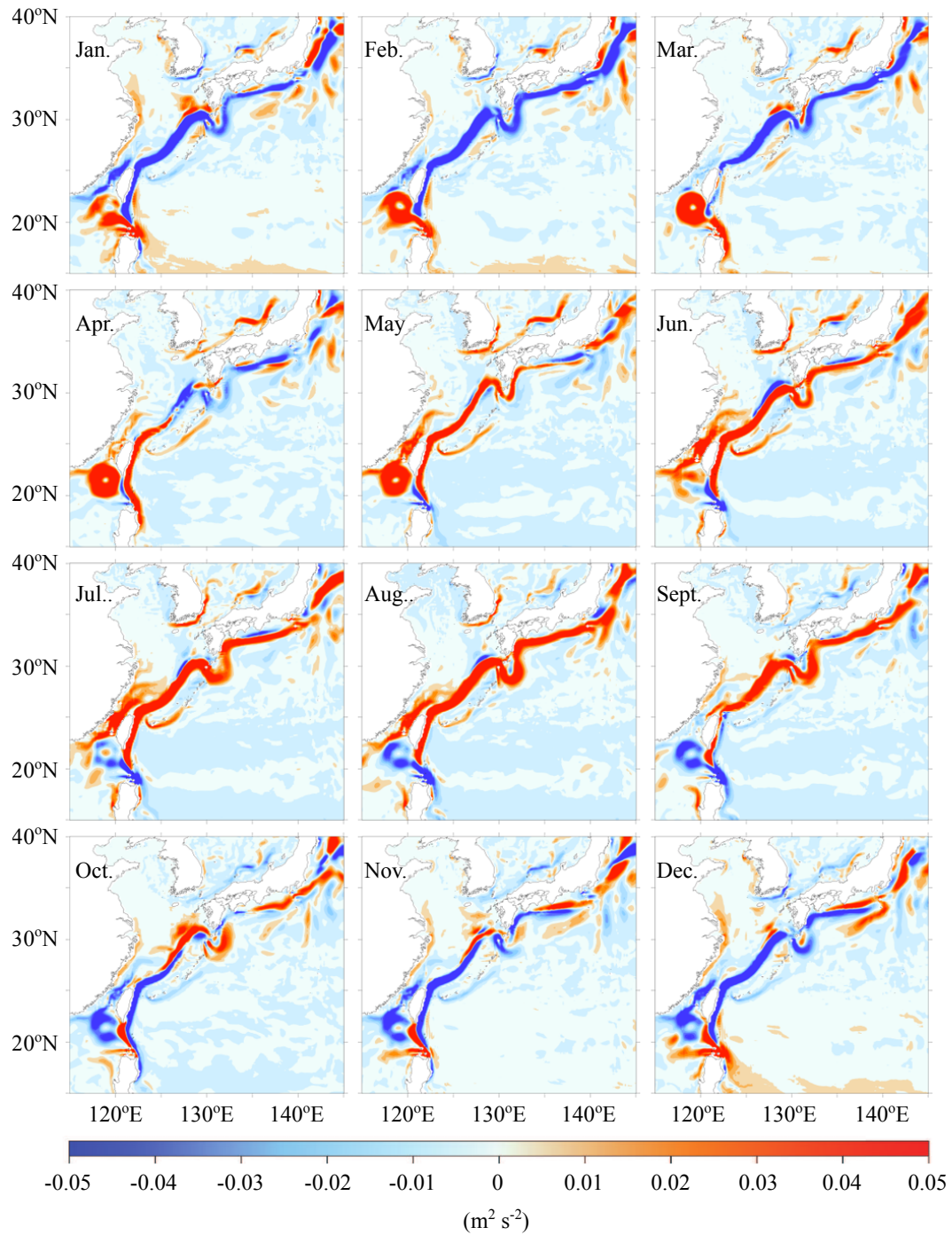


FIG. 10. Horizontal distributions of the monthly surface kinetic energy anomalies from annual means based on the results of Exp-1. The red (blue) color indicates positive (negative) anomalies.

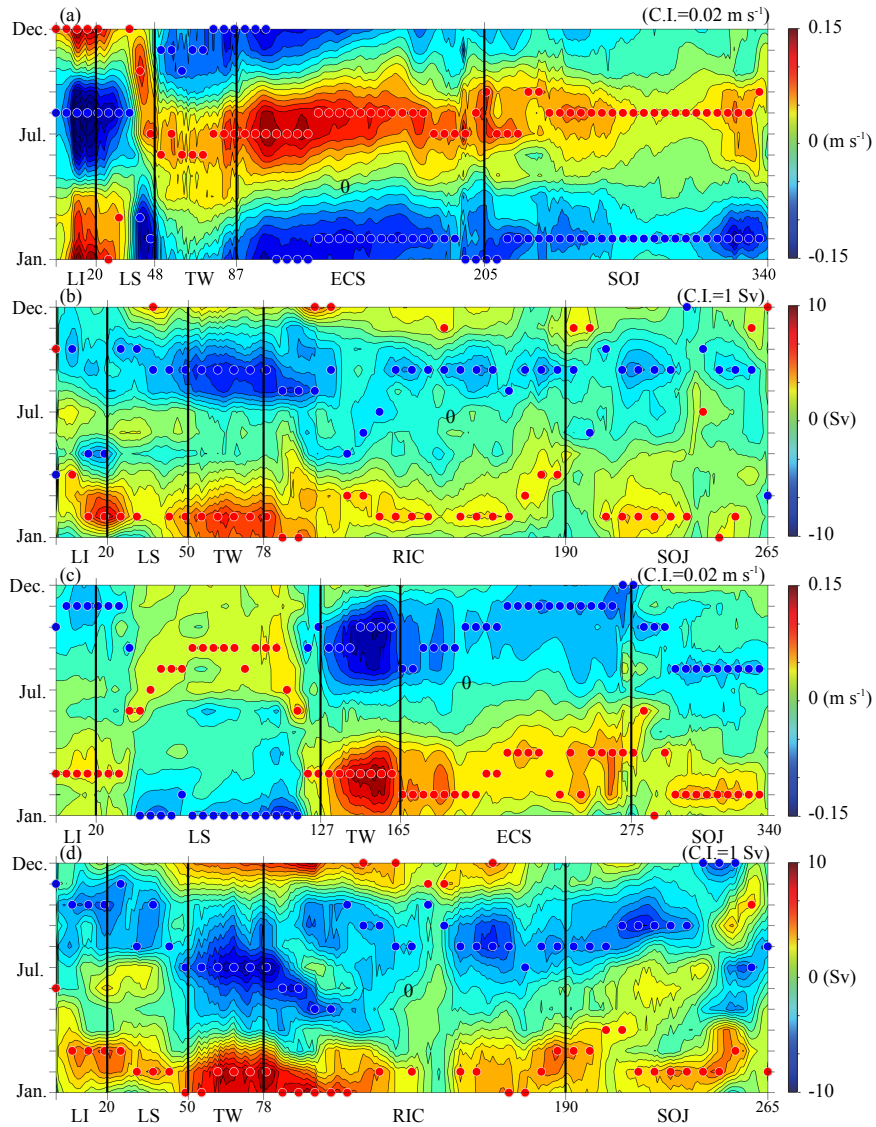


FIG. 11. Hovmöller diagrams of (a, c) the monthly surface velocity anomalies (see Figures 9a and 9b for the path) and (b, d) the monthly lower-layer volume transport anomalies integrated from 500 m depth to the bottom (see Figure 1 for the lower layer Kuroshio path), based on results from Exp-1 (a, b) and Exp-2 (c, d). The red (blue) dot at each location indicates a maximum (minimum) anomaly for the year. The horizontal axis indicates the cross section number, whose increment by 1 corresponds to the 10 km distance along the Kuroshio path. The vertical black lines are drawn to separate the individual regions. LI: east of Luzon Island; LS: east of Luzon Strait; TW: east of Taiwan; ECS: East China Sea; RIC: east of Ryukyu Island chain; SOJ: south coast of Japan.

from the CEMES altimeter data (Figure 3a) for the east of Luzon Island. More specifically, the maximum anomaly for the simulation appears from December to January but is actually observed in July in Figure 3a. In addition, the minimum anomaly for the simulation appears in August but is observed from September to December in Figure 3a. For the region around the Luzon Strait, the seasonal variation phases appear to be consistent between the simulation and observation, but exact comparisons are difficult because the simulated Kuroshio path near the Luzon Strait shifts horizontally due to the seasonal development of the loop current. As a result, it tends to divert significantly from the along-stream coordinate of the Hovmöller diagram (Figure 9a).

As mentioned above, simulated seasonal surface velocity variations are consistent with those observed for their phases over the region downstream of the Luzon Strait. However, their amplitudes are different from each other. For example, the simulated amplitudes in the ECS are larger than those near Taiwan and at the south coast of Japan, which results from the stronger stratification in the ECS than other regions for this model. The simulated seasonal velocity variations show a similar pattern from the sea surface to depths of approximately 400 m (figures not shown). Therefore, the seasonal features identified at the sea surface can be considered to represent the upper layer seasonal velocity variations.

To examine the simulated seasonal velocity variations in the lower layer, the velocities from 500 m depth to the bottom were integrated on the same cross-sections in the same manner shown in Figure 1. Figure 11b shows that the maximum seasonal variation in the lower layer appears mostly in winter (December to March) over the entire along-stream coordinate. However, the minimum values are concentrated in September at all simulated locations. These features closely resemble the observational features shown in Figure 5a over the broad area from the east of Luzon Island to the east of the Ryukyu Island chain (statistically significant at the 95% confidence level with $r > 0.78$). The averaged amplitude of the seasonal volume transport variation over this broad area

in the lower layer is approximately 8.5 Sv in our simulation, which is slightly smaller than that derived from the reanalysis data (~ 9.9 Sv).

In summary, the model successfully reproduced seasonal velocity variations in both the upper- and lower- layers. In the next subsection, the results from Exp-2, in which the wind stress over the entire WBR is removed (Figure 7b), are analyzed in detail.

4.1.3. *Driving force for the seasonal upper-layer velocity variations*

The seasonal velocity variations at the sea surface for Exp-2 show an essentially different variation pattern from that seen in the results of Exp-1. The kinetic energy anomalies over the entire Kuroshio path are mostly found to be positive during December to May and to be negative in other months (figure not shown). The maximum seems to be achieved around February rather than in July. The related Hovmöller diagram (Figure 11c) of surface velocity anomalies along the Kuroshio path (Figure 9b) clearly shows that the maximum anomalies no longer appear in July over the entire Kuroshio path, except for around the Luzon Strait. It is worth pointing out that in Exp-2, the Kuroshio takes a quasi-stationary looping path in the Luzon Strait (Figure 9b), which tends to diminish during the January to June period and to mature in the July to December months. These seasonal variations in loop currents may be explained by the mechanism proposed by Sheremet (2001). Specifically, the loop current, which is formed from the western boundary current at the gap on the continental slope, favors the weak current upstream of the gap. On the contrary, the leap current favors the strong current upstream of the gap. The seasonal velocity variations in the lower layer are relatively unaffected by the removal of the wind stress from the entire WBR. The integrated volume transports from 500 m depth to the bottom (Figure 11d) reach a maximum in winter (February to March) and a minimum in late summer (August to September). These features are almost the same as those obtained from Exp-1, except that the month when the minimum

anomalies appear for Exp-2 is delayed by approximately one month and the averaged amplitude over the entire along-stream coordinate for Exp-2 (~ 10.5 Sv) is somewhat larger than that in Exp-1 (~ 7.5 Sv) (statistically significant at the 95% confidence level for every area with $r > 0.79$).

A further look at the seasonal surface velocity variation for Exp-2 (Figure 11c) shows not only that the July maximum disappears over the entire Kuroshio path but also that a seasonal variation with a maximum in March and a minimum in September appears near the area east of Taiwan and propagates into the ECS. The seasonal volume transport variation in the lower layer (Figure 11d) also increases in amplitude near the area east of Taiwan comparing to that in Exp-1 (Figure 11b). This difference between Exp-1 and Exp-2 results from two parts: one is caused by the removal of the wind stress over the entire WBR, and the other is caused by the generation of artificial wind stress curl near the area where the wind stress suddenly decreases to zero (Figure 7b). Such effects can be approximately evaluated by comparing the Sverdrup volume transport for Exp-1 (Figure 12a) and that for Exp-2 (Figure 12b). Here, to obtain the Sverdrup volume transports, we integrated the wind stress curl over the area from 140° E (near the Izu-Ogasawara Ridge) to the western boundary (near the location of 3500 m isobath in Figure 1), considering the blocking effect of westward-propagating barotropic Rossby waves caused by the Izu-Ogasawara Ridge (see Section 5b for the discussion about determining the integration area). The overall feature of the seasonal variations in Sverdrup transport for Exp-2 (Figure 12b) is almost consistent with that for Exp-1 (Figure 12a): a maximum in December-January and a minimum around August (statistically significant at the 95% confidence level for every area with $r > 0.75$). However, the result of Exp-2 differs in that it (Figure 12c) shows a maximum in November-December and a minimum around June, especially east of Taiwan. Such a difference weakens (intensifies) the seasonal velocity variations associated with a summer (winter) maximum in the upper (lower) layer for Exp-2. We confirm that this difference is mainly caused by the generation of artificial wind stress curl rather

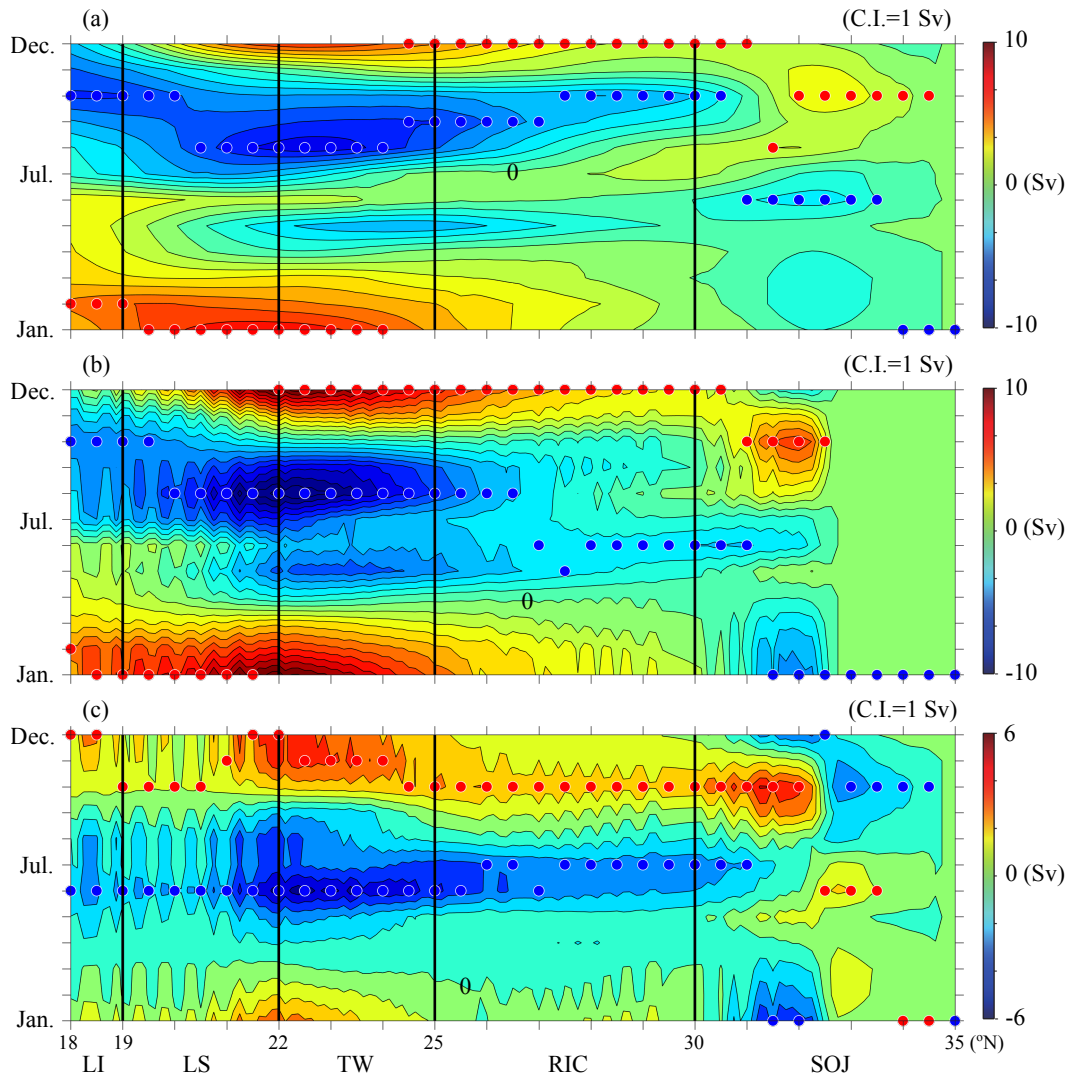


FIG. 12. Hovmöller diagram of the seasonal variations in Sverdrup transport, calculated at each latitude with wind stress curl over the area from 140° E (near the Izu-Ogasawara Ridge) to the western boundary (approximately, the location of 3500 m isobath shown in Figure 1): (a) the wind stress scenario used in Exp-1, (b) the wind stress scenario used in Exp-2, and (c) the difference between (a) and (b) (the latter minus the former). The horizontal axis indicates the latitude between 18° N and 35° N. LI: east of Luzon Island; LS: east of Luzon Strait; TW: east of Taiwan; RIC: east of Ryukyu Island chain; SOJ: south coast of Japan.

than the removal of wind stress curl over the entire WBR, comparing two cases in which wind stress curl is integrated to the western boundary of the North Pacific and to the eastern edge of the WBR (figure not shown). To derive proper conclusions for the impact of local wind stress on the seasonal velocity variations with a July maximum in the upper layer, Exp-3 and Exp-4 are conducted, in which the influence of the artificial wind stress curl is largely reduced in the ECS.

The features of the seasonal velocity variations at the sea surface for Exp-3 (no wind stress in the ECS) differ from those for Exp-1: The July and August maxima in the ECS, which are detected in Exp-1 (Figure 13a), almost disappear in Exp-3 (Figure 13b with the aid of Figure 9c). Furthermore, the artificial seasonal surface velocity variations, which have a maximum in March and a minimum in September for Exp-2 (Figure 11c), do not appear in the ECS for Exp-3. This is because the Ryukyu Island chain largely blocks the intrusion of the westward-propagating barotropic Rossby waves into the ECS so that the influence of the artificial wind stress curl is largely reduced in the ECS. It was confirmed that such a blocking effect on the seasonal velocity variations along the zonal band at $\sim 26^\circ$ N (figure not shown). The results of Exp-3 provide clear evidence that the local wind stress over the Kuroshio is a main driving force for the seasonal surface velocity variation for the Kuroshio in the ECS.

Comparing Exp-3 with Exp-1, downstream propagations of the seasonal signal along the Kuroshio path are discussed. Figure 13b shows that the seasonal surface velocity variations east of Taiwan for Exp-3 are almost the same as those for Exp-1. Specifically, the maximum appears in July, and the minimum appears in December and January. This seasonal signal does not penetrate into the ECS strongly. Unlike the upstream region, the propagation tendency from the ECS to the south coast of Japan cannot be discussed properly because the surface velocity field east of Tokara Strait (Figure 7c) for Exp-3 is exposed to the influence of artificial wind stress curl, as in Exp-2.

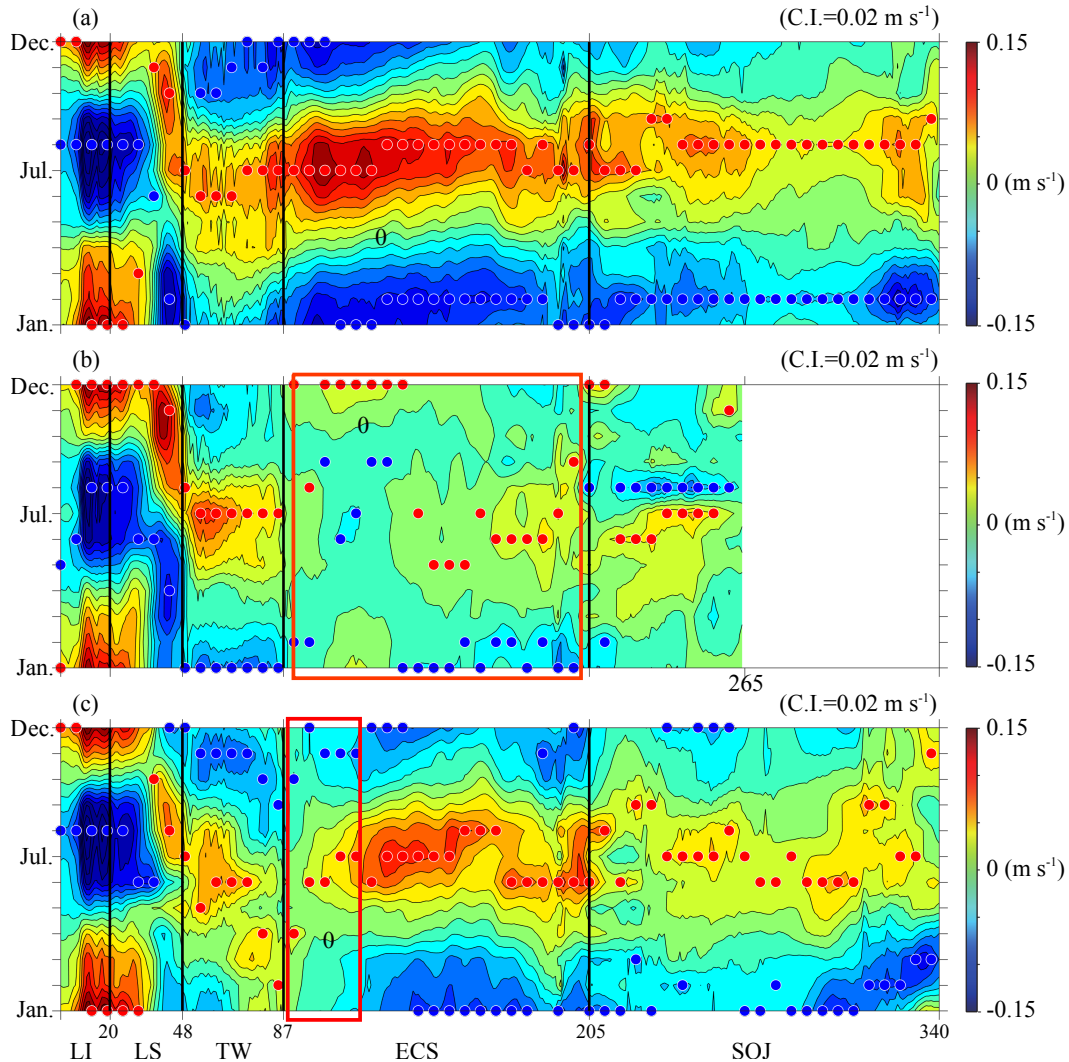


FIG. 13. Hovmöller diagrams of the monthly surface velocity anomalies from the annual means over the entire Kuroshio path from (a) Exp-1, (b) Exp-3 and (c) Exp-4. The cross-sections for estimating along-stream velocity components are defined for each experiment using its annual mean state (see Figure 9 for the path). The horizontal axis indicates the cross section number; its increment by 1 corresponds to the 10 km distance along the Kuroshio path. The vertical black lines are drawn to separate the individual regions. LI: east of Luzon Island; LS: Luzon Strait; TW: east of Taiwan; ECS: East China Sea; SOJ: south coast of Japan. The areas delimited by red boxed indicate the areas where wind stresses were removed.

More detailed development processes for seasonal surface velocity anomalies are further examined in the ECS. Since the seasonal variation amplitude is largest around the area northeast of Taiwan in the ECS, Exp-4 (no wind stress near north of Taiwan) is performed to determine how much seasonal wind stress variations around this area affect those variations in its downstream area through advection. The results of Exp-4 (Figure 13c) show that, except for the area where wind stress has been removed, seasonal velocity variations with summer maximum and winter minimum still exist, even though their amplitudes over the downstream area to the northeast of Taiwan are approximately 20% smaller than those in Exp-1 (Figure 13a). This indicates that seasonal surface velocity variations for the Kuroshio in the ECS are primarily caused by local responses to the wind stress upon the current and secondarily influenced by remote responses due to downstream advection. In addition to the mechanism for the ECS, it is difficult to prove such a mechanism for the entire Kuroshio region because the velocity field in other regions is exposed to the influence of artificial wind stress curl associated with the removal of the wind stress within the WBR. However, as the seasonal surface velocity variations have a similar seasonal feature over the entire Kuroshio path (see Exp-1), it is natural to infer that the local wind stress is a primary driving force not only in the ECS but also over the other Kuroshio regions.

4.1.4. *Hypothesis for the seasonal upper-layer velocity variations*

Historically, the seasonal volume transport variations for the Kuroshio and the Florida Current, both of which are characterized by a maximum in summer and a minimum in winter, have been primarily explained using two different mechanisms. The first is the Sverdrup response associated with the bottom topographic effects, which includes the JEBAR, e.g., by Sakamoto and Yamagata (1996) and Kagimoto and Yamagata (1997) for the Kuroshio, and Anderson and Corry (1985) and Greatbatch and Goulding (1989a) for the Florida Current. The other is the coastal response

involving the processes of coastal upwelling/downwelling and the process of equatorward anomaly propagation along the coast by barotropic waves, e.g., Czeschel et al. (2012) for the Florida Current. However, to the best of our knowledge, there have been no similar articles published on the Kuroshio, even though Kubota et al. (1995) proposed a response within the WBR that focused on vorticity input over the continental slope that was caused by seasonal along-slope wind stresses rather than coastal upwelling/downwelling. Whether these mechanisms are responsible for the results obtained from the numerical experiments are discussed below.

Based on the observational data analyses and the numerical experiment results, It was shown that seasonal velocity variations in the upper and lower layers are approximately 180° out of phase for the Kuroshio. This suggests that seasonal variations in volume transport, which are an integration of upper- and lower-layer velocities, are driven by the combined effect of different mechanisms. This factor is why the dynamics are examined underlying the velocity fields at different depths instead of using the volume transport in this study. It also suggests that the flow-topography interaction is not an essential mechanism, at least for seasonal upper-layer velocity variations of the Kuroshio, because both the observed and simulated variations are regarded as surface-intensified mode responses over the entire current.

For the coastal process, Czeschel et al. (2012) showed that seasonal volume transport variations of the Florida Current are predominantly related to coastal upwelling/downwelling signals that are propagated by barotropic Rossby waves. If this hypothesis works for upper layer seasonal velocity variations in the Kuroshio, the process must involve the land boundary located to the west of the current. However, the result obtained in Exp-3 indicates that the Kuroshio seasonal upper-layer velocity variations in the ECS occur independently of that land boundary (south coast of Japan). Following these considerations, the coastal upwelling/downwelling process with respect to the seasonal upper-layer velocity variation for the Kuroshio was reduced.

A hint of the new mechanism may be derived from Nakamura et al. (2015), who showed that, based on observational data analysis and numerical experiments, the seasonal monsoon wind acting on the Kuroshio in the ECS (see Figure 6) produces a seasonal shift of the Kuroshio path via local processes. Specifically, the southwestward wind blowing against the Kuroshio in winter shifts the Kuroshio path inshore-ward. In contrast, the northeastward wind blowing along the Kuroshio in summer shifts the Kuroshio path offshore-ward. Assuming that the Kuroshio is a surface geostrophic jet with a double exponential velocity profile, they indicated that the nonlinear Ekman divergence over the jet inputs positive vorticity into the jet, while its convergence inputs negative vorticity into the jet. The positive vorticity input in winter weakens the surface velocity shear of the offshore side of the jet and strengthens that of the inshore side of the jet, resulting in an apparent inshore-ward shift of the jet, while the negative vorticity input in summer reverses the process. It is thus inferred that this hypothetical mechanism causes a clear shift of the current axis for the case in which the jet has a double exponential profile characterized by a symmetric structure on both sides of the current axis. In addition to the seasonal shift of the current axis, Nakamura et al. (2015) clearly indicated that seasonal variations in the surface velocity field tend to be clearer on the offshore side of the current axis (see Figure 7 in their paper). This means that the current speed, which is represented by the velocity averaged across the width of the current, exhibits a seasonal feature due to the nonlinear Ekman divergence (convergence) over the jet. This feature is consistent with the seasonal surface velocity variations shown in the present study (Figure 2). Furthermore, a similar feature can be found in Kagimoto and Yamagata (1997) (see Figure 16 in their paper). Specifically, the sea surface height on the offshore side of the Kuroshio in the ECS becomes higher in summer and lower in winter. We expect that the nonlinear Ekman divergence (convergence) may account for not only the current axis variations but also the variations in the magnitude of the seasonal surface velocity. This consideration requires an additional observational

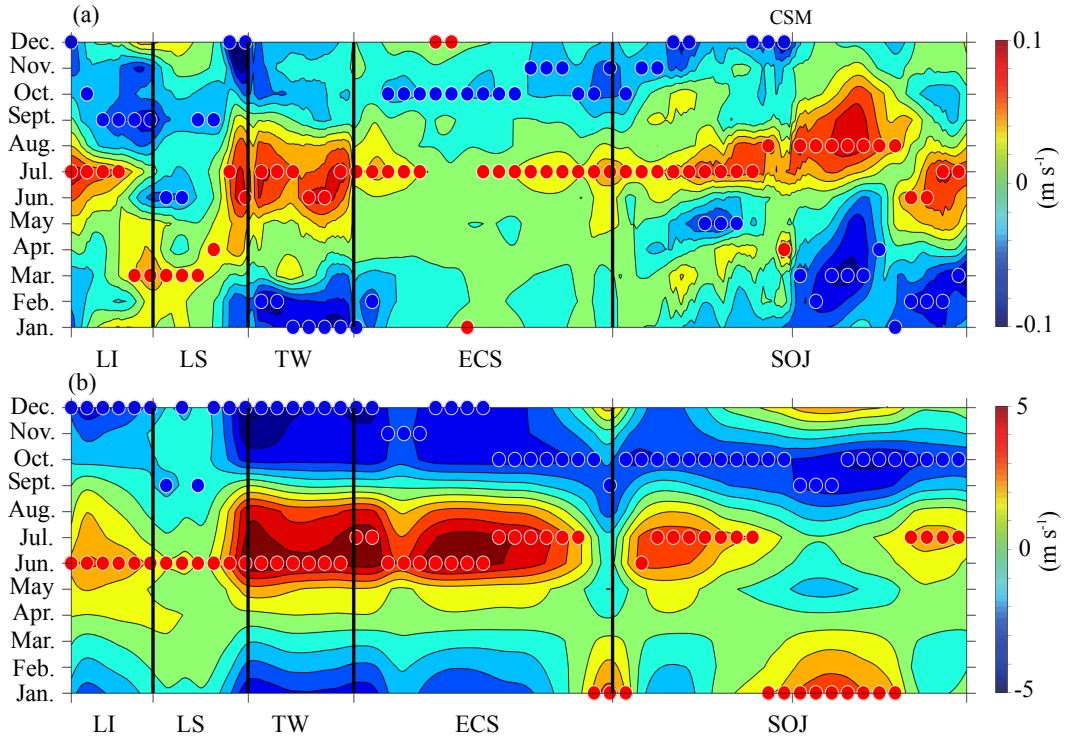


FIG. 14. Hovmöller diagrams of (a) the monthly surface velocity anomalies monthly along-stream current speed variations and (b) the 10-m wind velocity anomalies over the entire Kuroshio path. The anomalies are calculated based on the components in the direction of the upper layer Kuroshio path (red line in Figure 1). The current data are the Gridded Sea Level Anomalies and Absolute Dynamic Topography Heights and Current in Delayed-Time Two-Sat product from the Copernicus Marine Environmental Monitoring Service (CMEMS) for the period from 1993 to 2011 and the wind data are the Cross-Calibrated Multi-Platform wind vector analysis product on 0.25 deg grid, Version 2.0, with the same time period as that of the altimeter data. The vertical black lines are drawn to separate the individual regions. LI: east of Luzon Island; LS: Luzon Strait; TW: east of Taiwan; ECS: East China Sea; SOJ: south coast of Japan, CSM: Cape Shionomisaki.

data analysis to clarify the relationship between the surface Kuroshio velocity and the along-stream wind stress upon the Kuroshio.

Figure 14 shows a comparison between the monthly surface velocity anomalies (the same as Figure 3a) and the monthly 10-m wind velocity anomalies, which are estimated by averaging the normal components on each cross section along the upper-layer Kuroshio path (red line in Figure 1), over the entire Kuroshio path. The seasonal variations of the surface velocity anomalies and those of the 10-m wind velocity anomalies are almost coherent with a tendency of the summer maximum over the entire Kuroshio path, except for the areas near the Tokara Strait and downstream of Cape Shionomisaki where strong westerly winds blow in winter (figure not shown). Besides, the appearances of maximum surface velocity anomalies are delayed by about one month to those of maximum 10-m wind velocity anomalies over most areas of the Kuroshio path. On the other hand, the minimums for both the surface velocity and 10-m wind velocity anomalies appear in autumn (October) in the ECS while during the period from autumn to winter in other areas. These results imply that the seasonal upper-layer velocity variations in the Kuroshio may be explained as the response to the along-stream winds upon the Kuroshio through the nonlinear Ekman process. A detailed investigation of this hypothetical mechanism is provided in Chapter 5.

4.2. Driving mechanism for the lower-layer velocity variations

As shown in Figure 5a, the seasonal volume transport variation in the lower layer is mostly characterized by a winter maximum and autumn minimum over the broad area extending from the east of Luzon Island to the east of Kyushu along the eastern side of the Ryukyu Island chain. These seasonal features are similar to the results from Thoppil et al. (2016). By analyzing a global ocean reanalysis for the period 1993-2012, they showed that the Ryukyu Current system flowing east of the Ryukyu Island chain has a seasonal transport variation with a range of approximately 10 Sv (see Figure 19 in their paper). Following Sekine and Kutsuwada (1994), we know that a seasonal transport variation of this type is quite consistent in phase and amplitude with that of the Sverdrup

transport estimated by integrating wind stress curl over the western North Pacific to the west of the Izu-Ogasawara Ridge (see Figure 2 in their paper). The essential dynamic underlying this consistency is the blocking effect of the westward-propagating barotropic Rossby waves caused by the Izu-Ogasawara Ridge.

As the Sverdrup transport is responsible for the total volume transport integrated over the entire water column, the seasonal volume transport variation in the lower layer (Figure 5a) cannot be directly explained by seasonal Sverdrup transport variation (Figure 12a). However, as shown in Figure 5, the volume transport variation in the lower layer (Figure 5a) has almost the same seasonal features as that of total volume transport variation (Figure 5b), except that the former has smaller amplitudes than the latter. Therefore, the consistency of seasonal variations between the lower-layer and Sverdrup volume transports can be checked by comparing seasonal variations in the total volume transport (Figure 5b) and Sverdrup transport (Figure 12a). The phases of the seasonal Sverdrup transport variations (Figure 12a) are similar to the seasonal total volume transport variations (Figure 5b) over the area from the east of Luzon Island to the east of the Ryukyu Island chain (statistically significant at the 95% confidence level for every area except for the east of Taiwan). Specifically, the maximum values of the Sverdrup transport are mostly present in winter (around December), even though a weak peak also appears around June, while the minimum values are found in autumn (around October) and spring (around April). The amplitude of the seasonal Sverdrup transport variation averaged along the western boundary south of 30° N is approximately 10.6 Sv, which is on the same order as the amplitudes of the total volume transport variation (~ 13.1 Sv) and the lower layer volume transport variation (~ 9.9 Sv) averaged over the broad area from the east of Luzon Island to the east of the Ryukyu Island chain. This suggests that seasonal velocity variations in the lower layer are mainly dominated by the barotropic response to wind stress curl over the area west of the Izu-Ogasawara Ridge. Furthermore, assuming that the

amplitude of seasonal transport variation can be simply transferred into that of seasonal barotropic velocity variation, its value is $\sim 0.013 \text{ m s}^{-1}$, using a current width of 220 km and a water depth of 3500 m corresponding to the isobath used as a lower-layer Kuroshio stream line (blue line in Figure 1). This amplitude is $\sim 12\%$ of that at the surface ($\sim 0.11 \text{ m s}^{-1}$ from Figure 3) and is probably the reason why seasonal velocity variations in the upper layer are dominated not by the Sverdrup response but by a local process in the WBR.

5. Proving the hypothesis for the seasonal upper-layer velocity variations

Following the discussion in Chapter 4, the exact details of the local wind mechanism will be investigated in this chapter using a simple numerical model and an analytical model. The numerical model is configured using the typical values in the ECS. However, since it was shown that the seasonal velocity variation with a summer maximum is a coherent feature spanning most of the areas over the entire Kuroshio path (section), it is considered that the mechanism examined in the ECS can also be applied to other areas over the entire Kuroshio path. A sudden wind in summer or autumn were used as the driving force of the model according to the following result: the seasonal variation in the along-stream current speed follows the seasonal variation in the along-stream 10-meter wind speed within a month (Figure 14). This means that the surface current speed of the Kuroshio in the ECS responds to a summer (July) or autumn (October) wind upon the Kuroshio almost without phase lag. The sudden wind forcing in summer or autumn is, therefore, applicable to the dynamical study on the seasonal velocity variation in the upper layer of the Kuroshio in the ECS and is a simple way to understand the essential dynamics underlying seasonal variation. Following this consideration, the response of the upper-layer velocity to sudden winds will be discussed.

5.1. Numerical experiments with idealized bottom topography

Since the most distinct seasonal features of the velocity variation in the ECS appear in summer and autumn, a rectilinear regional model based on the POM with an idealized continental slope is forced by a uniform northward and a southward wind stress, respectively. To simplify the discussion, the turbulent closure scheme is switched off in this model and the vertical viscosity is set to be a constant value of $1 \times 10^{-3} \text{ m}^2 \text{ s}^{-1}$. The f -plane approximation is applied for this model with a constant Coriolis parameter at 30°N . The model domain (Figure 15), which measured $700 \times 1000 \text{ km}$, is covered by a rectilinear orthogonal grid with a space interval of 5 km in both the zonal and meridional directions. There are 140 cells in the zonal direction, 200 cells in the meridional direction and 30 sigma levels in the vertical direction. The bottom topography (h_b) of the model domain is estimated using the following equation:

$$h_b = d_{max} - \left(\frac{d_{max} - d_{min}}{2} \right) \left[1 - \tanh \left(\frac{x - d_{cen}}{d_{wid}} \right) \right] \quad (1)$$

where, d_{min} and d_{max} are the minimum and maximum water depths in the domain, respectively. d_{wid} and d_{cen} are the width and center position of the bottom slope, respectively. The minimum depth (d_{min}) and maximum depth (d_{max}) are set at 200 m and 1000 m with respect to the typical values in the ECS. The bottom slope width (d_{wid}) is set to be 100 km . The center of the bottom slope (d_{cen}) is set at a position 300 km away from the western boundary.

Inflow/outflow conditions are applied for the lateral boundaries of this model. On the southern and northern boundaries, internal velocity components in the meridional direction are specified based on the equation of Xue and Mellor (1993):

$$V(x, z) = V_0 \exp \left(\frac{z}{z_s} - X_i^2 \right) \quad (2)$$

$$X_i^2 = \left[x - x_f \left(1 - \frac{z}{z_s \cdot A} \right) \right]^2 / x_d \quad (3)$$

$$A = A_o + 20z / H_d \quad (4)$$

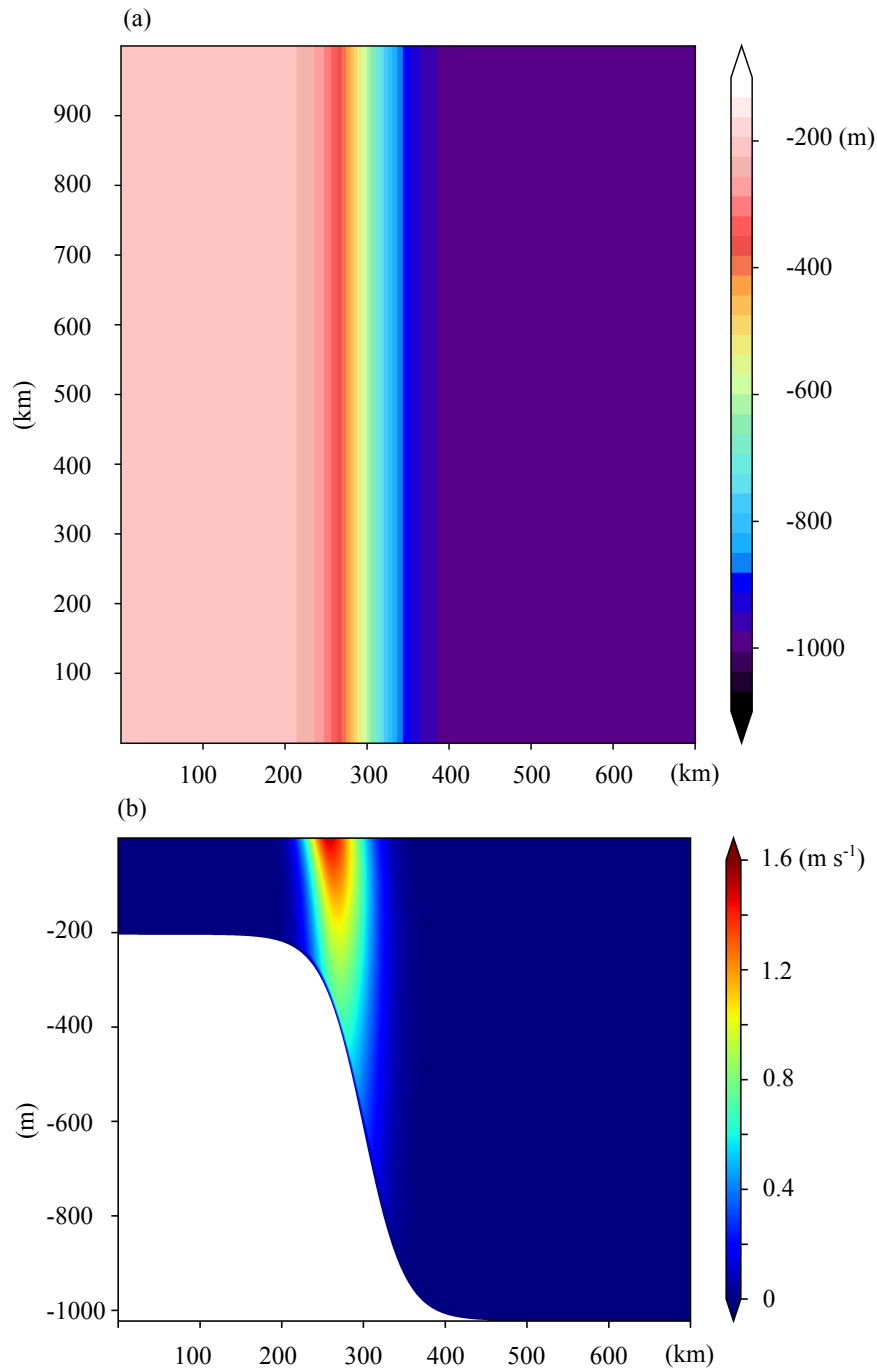


FIG. 15. (a) Horizontal distribution of the model domain with bottom topography and (b) the vertical velocity section at the southern boundary based on Eqs. (2-6). The minimum and maximum depths are set to 200 and 1000 m, respectively. The horizontal and vertical scales of the model domain are 700 km and 1000 km, respectively. The size of each grid in the zonal and meridional directions is 5 km.

$$x_d = x_{d1} - z(x_{d2} - x_{d1})H_d, (X_i \leq 0) \quad (5)$$

$$X_d = x_{d2}, (X_i > 0) \quad (6)$$

Table 2 summarizes the definitions and values used in these equations. External velocity components in the meridional boundaries are then calculated by integrating the internal velocity components from the sea surface to the bottom. The volume transport on the northern and southern boundaries is approximately 30.4 Sv, which corresponds to observations (~ 27 Sv) (Ichikawa and Beardsley 1993). On the western and eastern boundaries, only the external velocity components in the zonal direction are specified according to the Ekman transport, i.e., $\frac{\tau}{\rho f}$, where τ is the meridional wind stress component, ρ is the density of the sea water, which is set to 1000 kg m^{-3} , and f is the Coriolis parameter at 30°N . Upstream conditions are applied for salinity and temperature on all boundaries. Salinity is set to be a fixed value of 34.5. The vertical sections of temperature on the southern and northern boundaries are estimated according to the thermal wind relation with an assumption of a linear density-temperature relation using the equation:

$$\frac{\partial T(x, z)}{\partial x} = \frac{f \rho_0}{g \alpha} \frac{\partial V(x, z)}{\partial z} \quad (7)$$

where f is the Coriolis parameter, g is the gravitational acceleration, ρ_0 is a reference density of 1000 kg m^{-3} , α is a thermal expansion coefficient of $-0.25 \text{ kg m}^{-3} \text{ m}^\circ \text{C}^{-1}$ at 18.5°C , V is estimated velocity according to Eq. (2). Eq. (7) is then integrated from the western boundary to the eastern boundary of the model domain. The temperature profile on the western boundary is given by the equation:

$$T_e = 25 \exp(-2z/d_{max}) \quad (8)$$

To suppress noise near the boundaries, sponge layers with a length of 700 km and a width of 100 km are set at the northern and southern boundaries. Relaxation timescales increase linearly from zero to 0.1 days towards the boundaries.

TABLE 2. Definitions and parameter values used in Eqs. (2)-(6).

Parameter	Definition	Value
V_0	maximum surface velocity of the current	1.5 m s^{-1}
z_s	rate of the velocity decrease with depth	500 m
x_f	location of the maximum surface velocity	257 km
A_0	seaward hilt of the maximum velocity	5
H_d	maximum depth of the model domain	1000 m
x_d	current width	75 km
x_{d1}	inshore current width	30 km
x_{d2}	offshore current width	45 km

The model ocean is integrated for 100 days in each experiment. It is initially run without wind stress for 50 days to obtain a stable Kuroshio, and then it is forced by a uniform (northward/southward) wind stress. The time steps for the external and internal modes are set to 12 s and 240 s, respectively. The Smagorinsky-type formulation, with a non-dimensional constant of 0.2, is used to calculate the horizontal kinematic viscosity (A_m) and the horizontal temperature/salinity diffusivity (A_h). The value of A_h/A_m is set to 0.2.

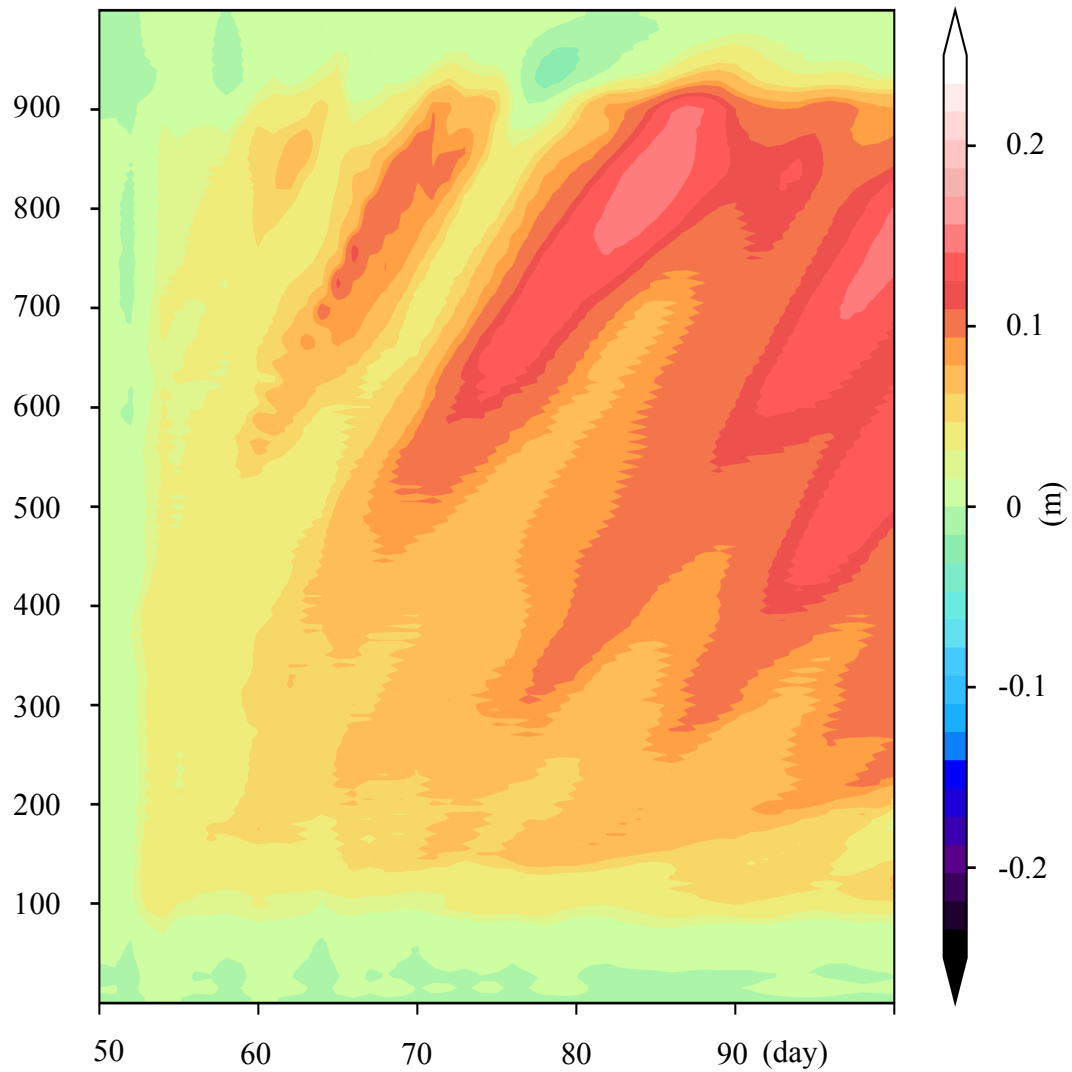


FIG. 16. Temporal and spatial variation in the sea surface height anomaly (SSHA) in summer relative to that in autumn. The SSHA is calculated using the data in the area between 250 and 350 km from the western boundary. The propagation speed of the signals from the southern boundary to the northern boundary is approximately 0.3 m s^{-1} .

5.1.1. *Checking the artificial signals*

The response to the local wind within the model domain is checked through the sea surface height anomaly (SSHA) between the location of 250 km and 350 km away from the western boundary. It can be seen that the SSHA near the southern boundary is almost unchanged for 50 days after the wind start to blow (Figure 16). This indicates that the variations within the model domain are hardly affected by the signals emanating from the southern boundary. In other words, the variations within the model domain are mainly due to the response of the jet to the local wind rather than due to the artificial signals from the southern boundary.

The variations in the SSHA (Figure 16) can be divided into two stages. The first stage lasts approximately 10–15 d after day 50, when the SSHA increases and no propagation signals appear over the entire model domain. The SSHA field is then adjusted in the second stage, which is dominated by downstream-propagation signals with a speed of 0.3 m s^{-1} . The downstream-propagation signals that originate approximately 200 km from the location reach the northern boundary around day 90; thus, the variations within the model domain take approximately 40 d to reach a steady state. This result is consistent with that from the observational data analysis, in which the surface velocity variations trail the wind speed variations by 1–2 months (Figure 14). The existence of the two different stages of variation is explained using the momentum equation. The first stage is dominated by the momentum balance between the local acceleration term and the forcing terms, whereas the second stage is dominated by the momentum balance between the nonlinear (advection) term and the forcing terms. Considering that blowing wind represented the steady state, we analyzed features in the velocity field on day 100, which represents the time 10 d after the first propagation signals reached the northern boundary (near day 90).

5.1.2. Performance of the numerical model

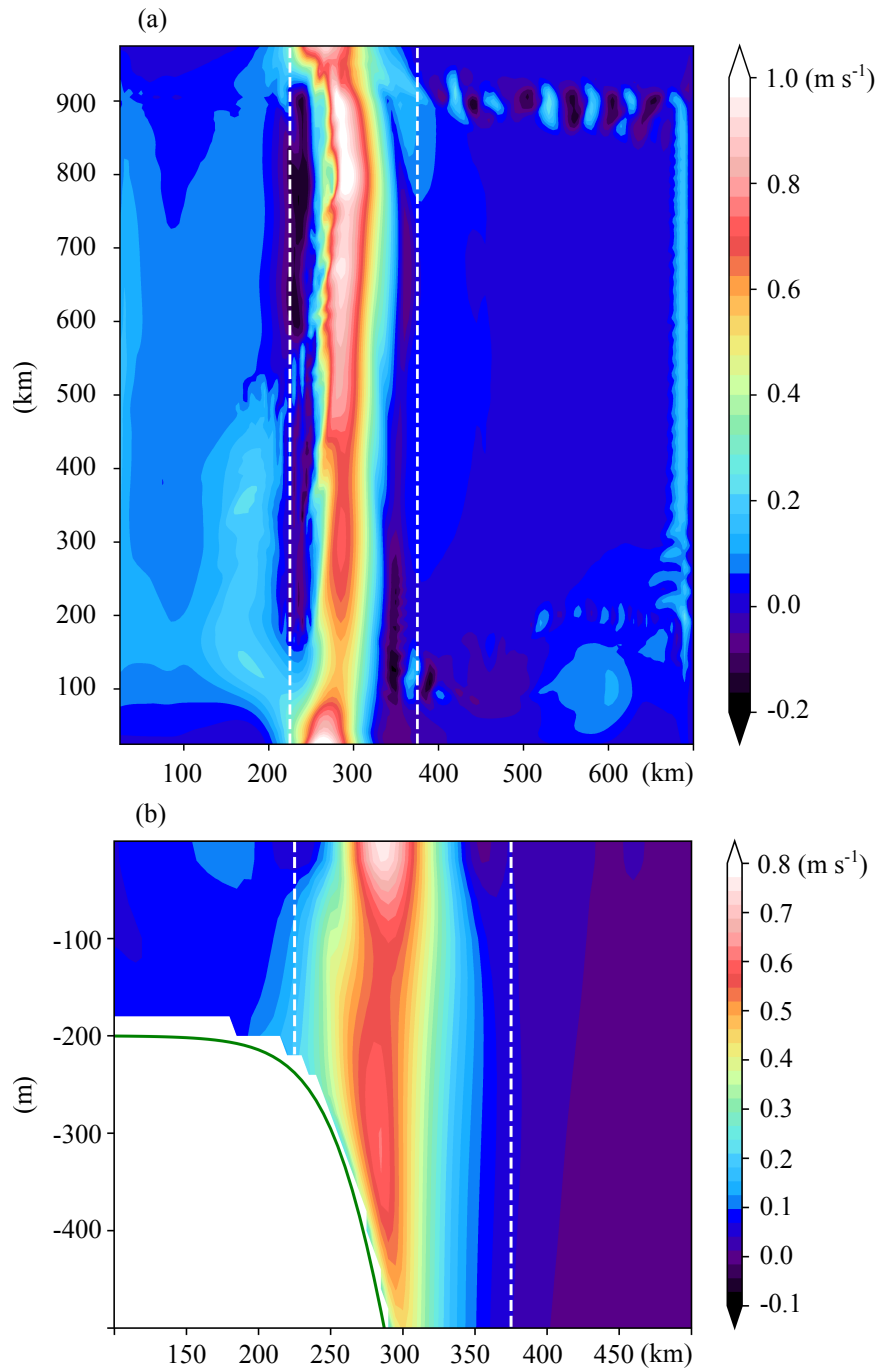


FIG. 17. (a) Horizontal distribution of the meridional velocity components near the sea surface (averaged 0-20 m) and (b) vertical section of the meridional velocity components on day 50. The vertical section is meridionally averaged over the area from 200 to 800 km. The area between the white dashed lines is regarded as the Kuroshio region.

Before checking the steady state features, the initial state features in the velocity field is shown on day 50, which is the day before the wind stress are applied. The horizontal distribution for the meridional velocity components (hereafter, v-components) near the sea surface (Figure 17a) shows that a main current is formed near the middle of the continental slope. On the western side of the main current, a small bifurcation current with a velocity approximately 0.2 m s^{-1} exists. Counter currents can be seen on both edges of the main current (dark blue shaded areas in Figure 17a). Such counter currents extend to a depth of approximately 30 m under the sea surface (Figure 17b) and the counter current on the western side is stronger than that on the eastern side. The vertical section of v-components (Figure 17b), which is averaged over the entire meridional length of the model domain, shows that there are two velocity cores: one near the sea surface and another near the bottom slope. These velocity cores are related to the stability of the current. For example, with a smaller shelf-edge depth than 200 m, the current becomes more stable and the number of velocity cores could reduce to only one.

The steady state features in the horizontal velocity field on day 100 under summer and autumn wind conditions are compared in Figure 18. The current summer path is located on the eastern side, and the surface velocity in summer is larger than that in autumn. Consequently, the response of the jet to sudden wind has two characteristics: variations in the current path and variations in the magnitude of the current velocity (speed). Nakamura et al. (2015) reported that the current path for the Kuroshio in the ECS moves to the inshore side (westward) in winter, when the local winds blow southward against the direction of the Kuroshio. This is consistent with the current path variations simulated under autumn wind condition in this study. On the other hand, the observed current speed variation averaged in the ECS has an amplitude (value in summer minus that in autumn) of 0.05 m s^{-1} (Figure 14). Furthermore, the amplitude of the simulated current speed variation is defined as the difference between the summer and autumn v-component velocities averaged over

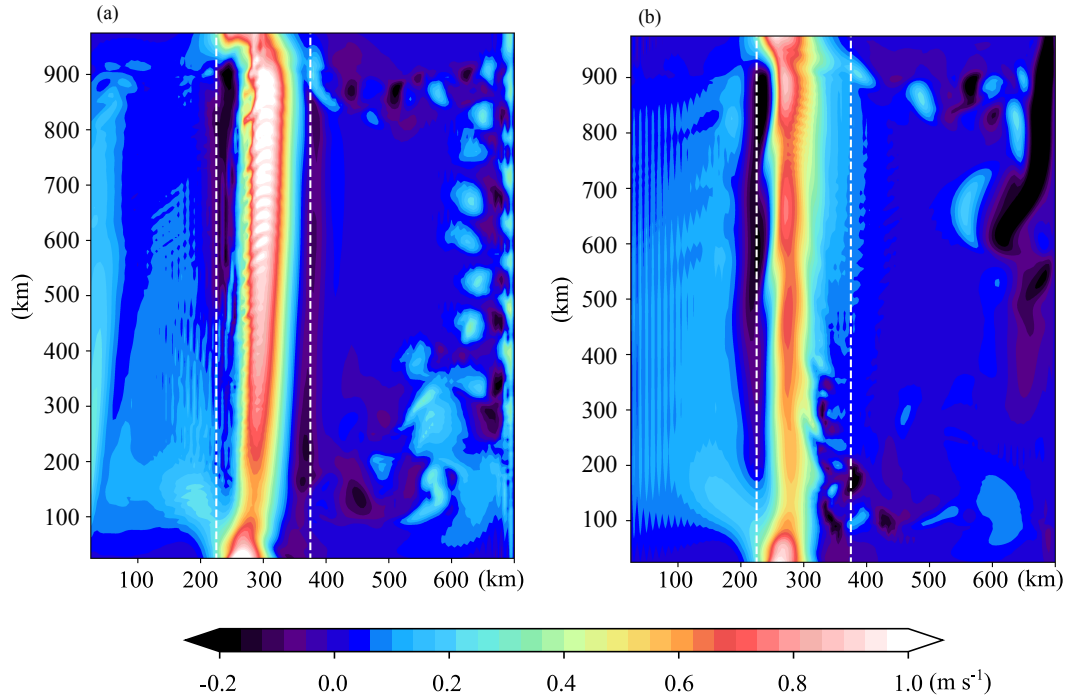


FIG. 18. Horizontal distributions of the meridional velocity components near the sea surface (averaged 0-20 m) for (a) summer and (b) autumn winds on day 100. The area between the white dashed lines is regarded as the Kuroshio region.

the width of the jet (150 km), which ranges from 225–375 km (dashed white lines in Figure 18) from the western boundary. The current speed variations in Figure 18 (summer values minus autumn values) have a mean value of 0.08 m s^{-1} , which is averaged in the meridional direction over the area from 200–800 km and is of the same order as the observed amplitude of 0.05 m s^{-1} (Figure 14).

The steady state features under the sea surface are checked through the vertical section of density anomalies (Figure 19, the vertical section is meridionally averaged over the area from 200–800 km) and calculated by subtracting the autumn density from the summer density. Two areas with large-amplitude anomalies reach a depth of approximately 150 m within the jet. The areas on the western and eastern sides of the jet are characterized by positive and negative anomalies,

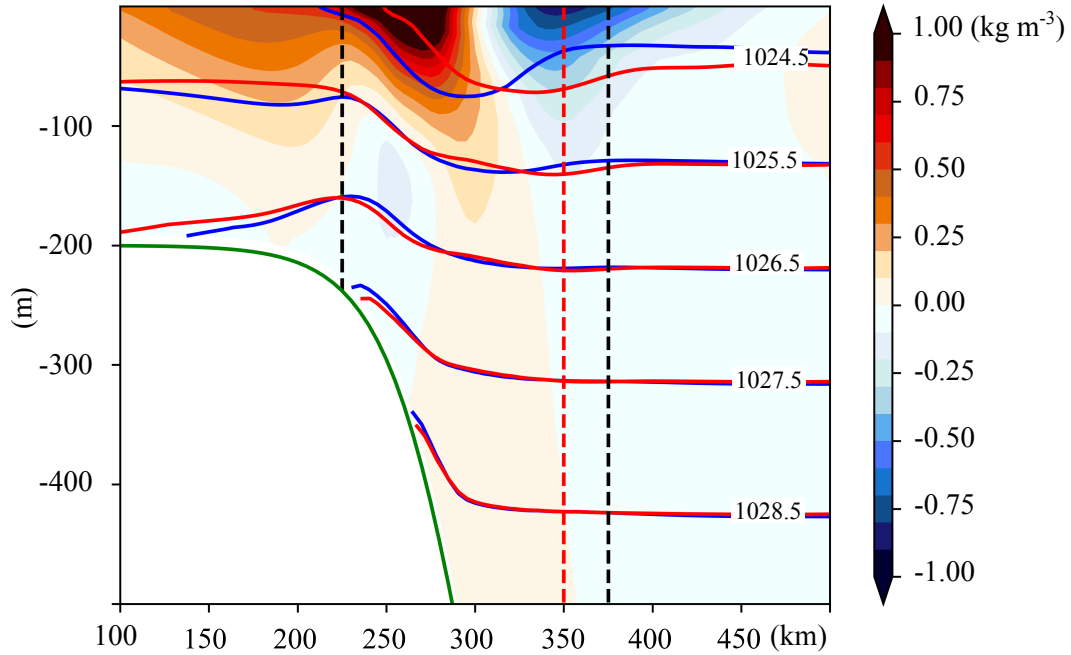


FIG. 19. Vertical section of the density anomaly (summer minus autumn) on day 100. Red (blue) contour indicates the isopycnal in summer (autumn). The area between the black dashed lines is regarded as the Kuroshio region. The vertical section is averaged over the area from 200 to 800 km. The red dashed line is a reference line used to estimate the order of the vertical shift in the 1024.5 kg m^{-3} isopycnal due to nonlinear Ekman pumping. The contour interval is 1.0 kg m^{-3} .

respectively. This distribution is attributed to horizontal and vertical shifts in the thermocline. On the one hand, the horizontal thermocline shift is associated with the horizontal shift of the jet and regarded as the current path variation. On the other hand, the vertical thermocline shift that occurs locally within the jet generates a horizontal pressure gradient variation and induces a change in the current velocity field over the width of the jet that corresponds to current speed variations. Therefore, the distribution of the density anomalies (Figure 19) indicates that the current path and speed variations exist near the sea surface and to depths of $\sim 150 \text{ m}$ in the jet.

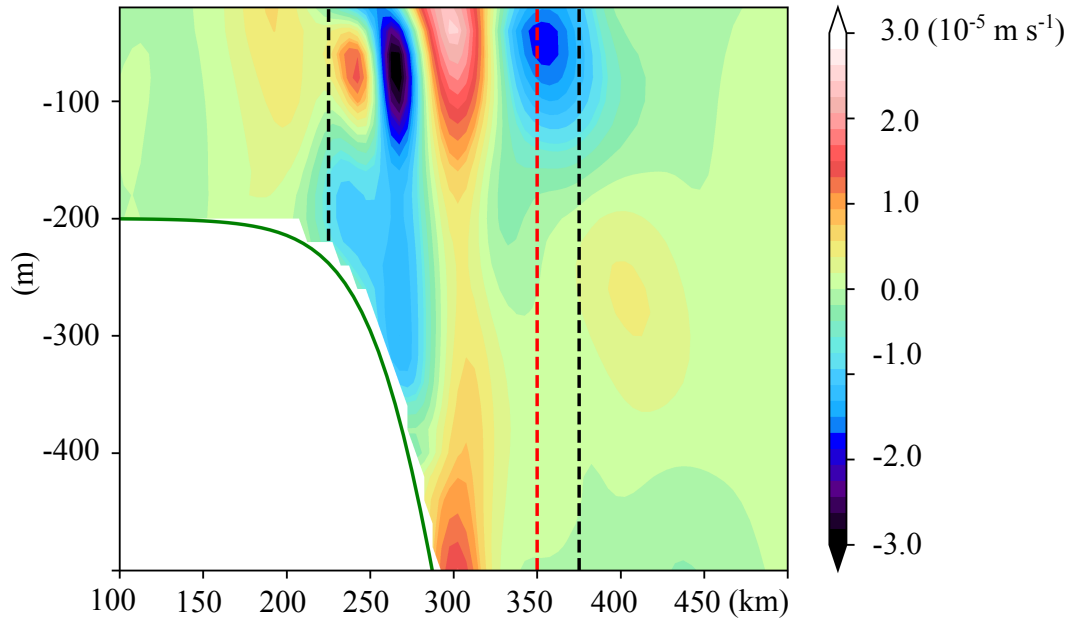


FIG. 20. Vertical section of the time-averaged (day 50-100) w anomaly (summer minus autumn) which is meridionally averaged over the area from 200 to 800 km. The red dashed line is a reference line used to estimate the order of the vertical shift of the 1024.5 kg m^{-3} isopycnal due to nonlinear Ekman pumping.

This study considered a hypothesis that the current speed variation is forced by thermocline variation due to nonlinear Ekman pumping. To check this hypothesis, the vertical section of the vertical velocity (hereafter, w) anomalies (values in summer minus those in autumn), which are averaged in the period from day 50 to day 100 and averaged over the entire meridional length of the model domain, was examined. The distribution of the w anomalies (Figure 20) has an approximately symmetric distribution; the summer (autumn) distribution near the sea surface is characterized by a positive (negative) anomaly near the center of the current and negative (positive) anomalies on the western and eastern sides of the jet. This feature exists to deeper depths in the jet; however, the negative w anomaly on the western side of the jet remains, whereas that on the eastern side disappears.

Comparing the vertical section of the w anomalies (Figure 20) and the density anomalies (Figure 19), it can be found that the distribution of the w anomalies is spatially consistent with the distribution of the thermocline variation: the thermocline is lifted up near the center of the Kuroshio where there is upwelling and it moves deeper on the offshore side of the jet where there is downwelling. Using a w anomaly value of $2 \times 10^{-5} \text{ m s}^{-1}$ near a depth of 100 m at a location of 350 km (red dashed line in Figure 20), it can be estimated that the nonlinear Ekman pumping produces a depression of 35-86 m in the thermocline, assuming that the response time is in the range of 20 to 50 days. The estimated thermocline displacement is within the same order as the simulated thermocline displacement between summer and autumn (~ 40 m) at a location of 350 km (Figure 20). Therefore, the nonlinear Ekman pumping is considered to drive thermocline variation, which causes current speed variation.

Since the analytical model is forced by nonlinear Ekman pumping formula that was introduced in Nakamura et al. (2015) (Eq. (12)), whether this formula can be used for estimating the simulated results properly was checked. Using the w anomalies at 20 m depth in Figure 20, the simulated result (red line) and the estimated result (blue line) based on Eq. (12) are compared in Figure 21. The w_e estimated from Eq. (12) (green line) is within the same order of magnitude as that obtained from the model output (red line) but exhibits an asymmetrical distribution with a larger amplitude on the western side of the jet. On the other hand, w_e estimate using the non-linearized formula (Eq. (13), blue line) is close to the nearly symmetrical distribution of the model output. These results indicates that more approximations are necessary to predict the vertical velocity at the bottom of the Ekman layer using Eq. (12). In the following section, the details of the approximations for Eq. (12) are discussed.

5.2. Analytical model used to explain the hypothesis

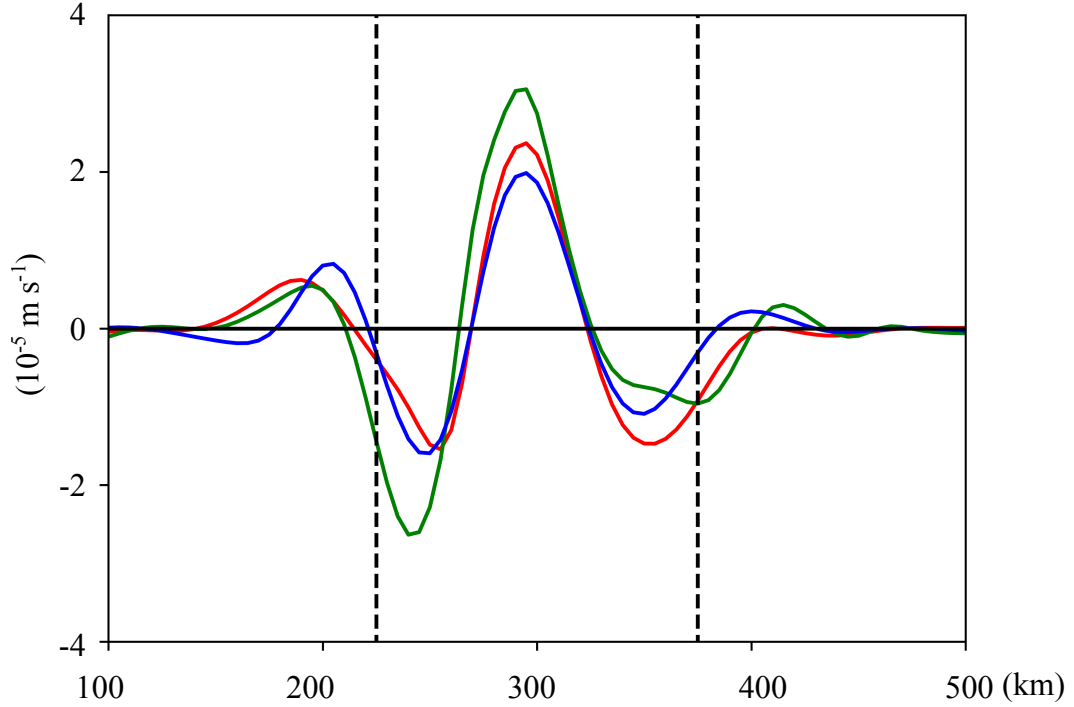


FIG. 21. Time-averaged (day 50-100) w anomalies (summer minus autumn) at 20 m depth (red line) and the estimation based on Eqs. (12) and (13) (green and blue lines). The area between the black dashed lines is regarded as the Kuroshio region.

The considered hypothesis is that the current speed variation is forced by thermocline variation due to nonlinear Ekman pumping. Here, since the Ekman pumping velocity is stated as a nonlinear formula, the upwelling/downwelling within the jet is referred to as ‘nonlinear Ekman pumping’ in this study. To examine this mechanism, a rigid-lid reduced-gravity model is constructed based on the nonlinear Ekman pumping formula (Nakamura et al. 2015). Considering the variations in the vertical velocity section, which are uniform in the meridional direction, the linearized equations system is:

$$\frac{\partial u}{\partial t} - fv = -g' \frac{\partial h}{\partial x} \quad (9)$$

$$\frac{\partial v}{\partial t} + fu = 0 \quad (10)$$

$$\frac{\partial h}{\partial t} + H \frac{\partial u}{\partial x} = -w_e \quad (11)$$

where h is the thickness of the upper layer; H is the mean thickness of the upper layer; g' is the reduced gravitational acceleration; f is the Coriolis parameter; x and y are the coordinates in the zonal and meridional directions, respectively; u and v are the zonal and meridional velocity components, respectively; and w_e is the nonlinear Ekman pumping velocity that is used in Nakamura et al. (2015):

$$w_e = -\frac{\tau_y}{f^2 \rho_0} \frac{\partial^2 v}{\partial x^2} \quad (12)$$

where, w_e is the vertical velocity at the bottom of the Ekman layer, τ_y is the meridional component of the wind stress, f is Coriolis parameter, ρ_0 is the sea water density, and v is the meridional component of the jet velocity. Eq. (12) is the linearized expression of the nonlinear Ekman pumping velocity from Nakamura et al. (2010):

$$w_e = -\frac{\partial}{\partial x} \left(\frac{\tau_y}{f^* \rho_0} \right), \quad (13)$$

where f^* is the effective Coriolis parameter (Niiler (1969)):

$$f^* = f + \frac{\partial v}{\partial x}. \quad (14)$$

The velocity components u , v and the thickness of upper layer h are decomposed as follows:

$$u = u_b + u_d \quad (15)$$

$$v = v_b + v_d \quad (16)$$

$$h = H + h_d \quad (17)$$

where u_b and v_b denote the background time-independent velocity components of the jet, u_d and v_d denote the deviation components of the jet velocity, and h_d denotes the deviation of the

thermocline thickness. Taking $\partial(10)/\partial x$ and using (11) yields the linearized potential vorticity (PV) conservation law as:

$$\frac{\partial}{\partial t} \left(\frac{\xi}{f} - \frac{h_d}{H} \right) \quad (18)$$

where ξ is the vorticity, which is defined as $\frac{\partial v_d}{\partial x}$. Assuming a geostrophic balance, ξ is represented with h_d as:

$$\xi = \frac{\partial g'}{\partial f} \frac{\partial^2 h_d}{\partial x^2} \quad (19)$$

Using the relation above, Eq. (16) can be rewritten as:

$$\frac{\partial}{\partial t} \left(R_e^2 \frac{\partial^2 h_d}{\partial x^2} - h_d \right) = w_e \quad (20)$$

Here, R_e is the Rossby deformation radius, which is defined as:

$$R_e = \frac{\sqrt{g'H}}{f}. \quad (21)$$

Eq. (20) shows that the nonlinear Ekman pumping generates the variations in the relative vorticity and the stretching of the water column. Integrating Eq. (20) with respect to t with the initial condition $h_d(t=0) = 0$, yields

$$R_e^2 \frac{\partial^2 h_d}{\partial x^2} - h_d = w_e \cdot t \quad (22)$$

The mechanism can be explained based on the solution of Eq. (22) for a given nonlinear Ekman pumping w_e and was used to discuss the dynamics for the current speed variations.

5.2.1. Assumptions for the analytical model

Eq. (22) explains the variation in the thermocline owing to nonlinear Ekman pumping and can be analytically solved if the nonlinear Ekman pumping velocity (w_e) is given as a particular function. The condition that must be satisfied by the jet profile to reproduce the real Ekman pumping distribution within the jet is that the jet profile is characterized by a convex profile (with negative

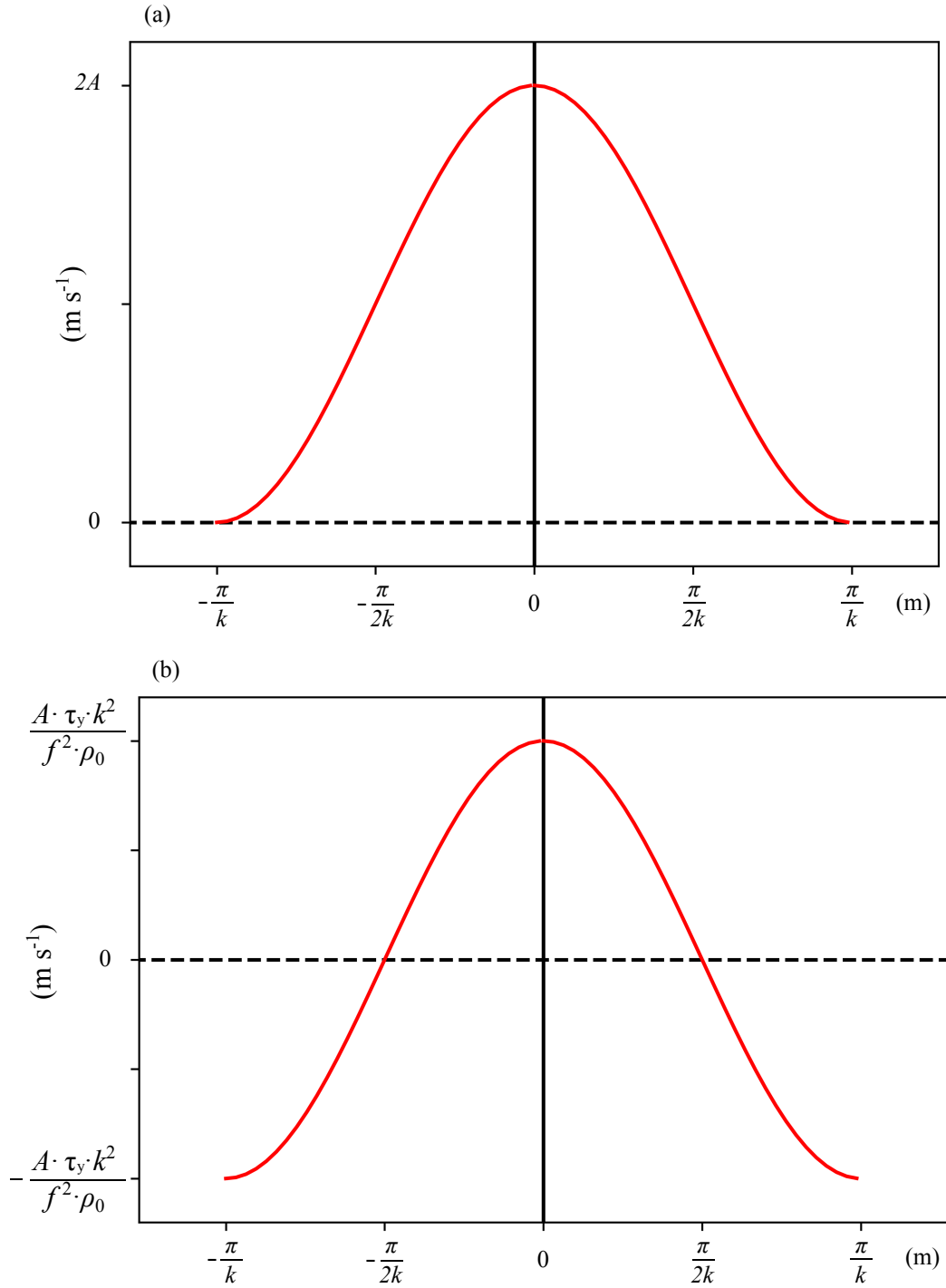


FIG. 22. (a) Velocity profile of a northward jet that is assumed as a function of cosine (Eq. 22). (b) Horizontal distribution of w_e according to Eq. (12).

curvature) around the jet axis and concave profiles (with positive curvatures) on the western and eastern sides. Further, the jet profile must be selected to provide an analytical solution to Eq. (22). Thus, we first assume a jet profile of the cosine function (Figure 22a) and examine whether the current speed variation can be explained by this assumption. The jet profile (v_b) is:

$$v_b = A(\cos(kx) + 1), \left(-\frac{\pi}{k} \leq x \leq \frac{\pi}{k}\right) \quad (23)$$

where k is the wavenumber and A ($A > 0$) is half of the current speed at the current axis (location of the maximum v -component over the width of the jet). According to Eq. (12), w_e is given as

$$w_e = k^2 B A \cos(kx), \left(-\frac{\pi}{k} \leq x \leq \frac{\pi}{k}\right) \quad (24)$$

Here, $B = \frac{\tau_y}{f^2 \rho_0}$. Considering a summer wind case with $\tau_y > 0$, the horizontal distribution of w_e within the width of the jet has a symmetrical horizontal distribution with upwelling near the center of the jet and downwelling on each side of the jet (Figure 22b). Such a distribution is similar to that of the model output (red line) shown in Figure 21. With Eq. (24), the solution (h_d) in Eq. (22) can then be derived analytically as:

$$h_d = h_d^0 + h_d^* \quad (25)$$

where h_d^0 and h_d^* are homogeneous and particular solutions for Eq. (22), respectively:

$$h_d^0 = C_1 t e^{\frac{x}{R_e}} + C_2 t e^{-\frac{x}{R_e}}, \quad (26)$$

$$h_d^* = -\left(\frac{B A k^2}{R_e^2 k^2 + 1}\right) \cos(kx) t. \quad (27)$$

Here, C_1 and C_2 are unknown constants. Assuming geostrophic balance, the variation of the thermocline can be converted into the velocity variation, as follows:

$$v_d = \frac{g'}{f} \frac{\partial h_d}{\partial x} \quad (28)$$

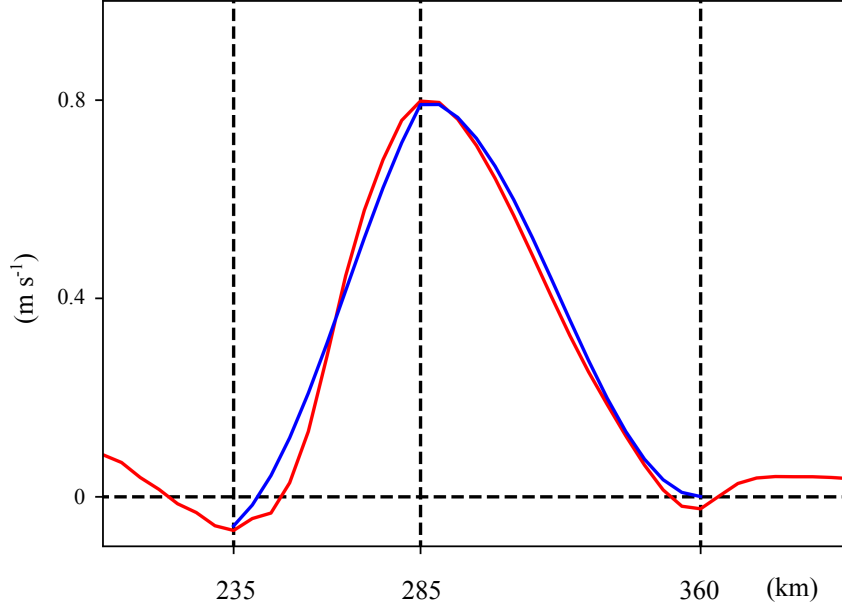


FIG. 23. Horizontal velocity profile of the jet (red line) near the sea surface (averaged at depths of 0-20 m) on day 50. The velocity profile is meridionally averaged over the area from 200 to 800 km. The blue line shows the curve-fitted result using a function given by Eqs. (30-31) for each side of the jet with particular condition (Eqs. (34-36)). Here, $V=0.8 \text{ m s}^{-1}$, $k_W=6.28 \times 10^{-5} \text{ m}^{-1}$, $k_E=4.19 \times 10^{-5} \text{ m}^{-1}$, $A_E=0.4$ and $c = d = 0$ are applied. A_W (~ 0.178) and b (~ 0.444) can be calculated using Eqs. (34) and (35), respectively. a (~ 0.051) is adjusted using the minimum values (at 235 km from the western boundary) on the western side of the jet.

so that:

$$v_d = - \left(\frac{BAk^3 g'}{R_e^2 k^2 f^2 + f} \right) \sin(kx)t \quad (29)$$

Here, because the particular solution satisfies the boundary condition—which requires the velocity on each side of the jet to be zero— $h_d = h_d^*$ is used. Eq. (29) is the velocity variation over the width of the jet owing to the nonlinear Ekman pumping velocity (w_e).

The response of the jet with the profile given by Eq. (29) is rotationally symmetrical with respect to $x=0$. Therefore, the current speed variation does not occur if Eq. (29) is integrated over the width of the jet. Therefore, the assumption of a symmetrical jet profile is not suitable for explaining the current speed variation, which requires assuming an asymmetrical jet profile. The asymmetrical jet profile can be confirmed from the numerical results (Figure 23). Namely, the wavelength (or wavenumber: k) on the western side of the jet is smaller (larger) than that on the eastern side. This feature is supported by observational results by a realistic numerical simulation result for the Kuroshio in the ECS (Figure 14 in Nakamura et al. (2010)). Next, we discuss the current speed variation with the assumption of an asymmetrical jet profile.

5.2.2. Explanations of the hypothesis based on an analytical solution

Considering that the wavenumber is larger on the western side of the jet, we assume a jet profile of:

$$v_b = A_W(\cos(k_W x) + 1) + ax + b, \quad (x < 0) \quad (30)$$

$$v_b = A_E(\cos(k_E x) + 1) + cx + d, \quad (x \geq 0) \quad (31)$$

where k_W and k_E ($k_W > k_E$) are the wavenumbers on the western and eastern sides of the jet, respectively. Instead of Eq. (23), Eqs. (30-31) are used for an asymmetrical jet profile, in which a linear velocity profile is added on each side of the jet to satisfy the continuity of w_e at $x = 0$.

According to Eq. (12), w_e is:

$$w_e = k_W^2 B A_W \cos(k_W x), \quad (x < 0) \quad (32)$$

$$w_e = k_E^2 B A_E \cos(k_E x), \quad (x \geq 0) \quad (33)$$

For the condition of $k_W \neq k_E$, the jet profile (v_b , Eqs. (30-31)) and the nonlinear Ekman pumping velocity (w_e , Eqs. (32-33)) are continuous at $x = 0$, with:

$$2A_W + b = V, \quad (34)$$

$$2A_E + d = V, \quad (35)$$

$$A_W k_W^2 = A_E k_E^2. \quad (36)$$

Here, V is the current speed at the current axis ($x = 0$). If V , k_W , k_E , and either A_W or A_E are given as parameters, the velocity profile of the jet is determined uniquely. According to the model result that w_e is nearly symmetrical to the current axis (Figure 21), this jet profile is regarded as a possible candidate. Amplitudes of w_e for both sides are replaced by a constant value, C ($C > 0$ for the summer case, and $C < 0$ for the autumn case), as follows:

$$k_W^2 B A_W = k_E^2 B A_E = C, \quad (37)$$

$$k_W \neq k_E, \quad (38)$$

so that w_e is written as:

$$w_e = C \cos(k_W x), \quad (x < 0) \quad (39)$$

$$w_e = C \cos(k_E x), \quad (x \geq 0) \quad (40)$$

If given Eqs. (39-40), the particular solution (h_d^*) on each side of the jet is:

$$h_d^* = - \left(\frac{C}{R_e^2 k_W^2 + 1} \right) \cos(k_W x) t, \quad (x < 0) \quad (41)$$

$$h_d^* = - \left(\frac{C}{R_e^2 k_E^2 + 1} \right) \cos(k_E x) t, \quad (x \geq 0) \quad (42)$$

Assuming a geostrophic balance, the velocity variation is:

$$v_d = - \left(\frac{C k_W g'}{R_e^2 k_W^2 f + f} \right) \sin(k_W x) t, \quad (x < 0) \quad (43)$$

$$v_d = - \left(\frac{Ck_E g'}{R_e^2 k_E^2 f + f} \right) \sin(k_E x) t, \quad (x \geq 0) \quad (44)$$

Eqs. (43-44) represent the velocity variation due to the nonlinear Ekman pumping velocity (w_e) on each side of the jet. This solution grows monotonically with time but reaches a steady state and includes the combined effect of advection and topographic Rossby wave propagation in the PV conservation law (Eq. (18)). The numerical model results show that a propagation signal emanating from the southern boundary reaches the northern boundary on day 90. Therefore, the time for this adjustment was approximately 40 d. The particular solution (h_d^*) is discontinuous at $x = 0$ and, therefore, an approximate solution for Eq. (22). Next, we examine Eqs. (43-44) for current speed change characteristics.

By integrating Eqs. (43-44) from 0 to $\frac{\pi}{k}$ and averaging over the length of $\frac{\pi}{k}$, the average current speed variation (v_a) on each side of the jet is:

$$v_a = \frac{2Cft}{H\pi} \left(\frac{k}{k^2 + \frac{1}{R_e^2}} \right) \quad (45)$$

where $k = k_W$ or $k = k_E$. Figure 24a shows the relation of v_a to k . Considering that $k_W > k_E$, the relation of v_a to k can be classified into three cases by comparing the cross-jet length scale ($L = \frac{1}{k}$) and the Rossby deformation radius (R_e). For L larger than R_e on both sides of the jet, i.e., $k_E < k_W < \frac{1}{R_e}$, v_a becomes larger as k increases. In this case, the current speed decreases in summer and increases in autumn, contradicting the results of the numerical model. In contrast, for L smaller than R_e on both sides of the jet, v_a decreases as k increases, yielding increases and decreases in current speed in the summer and autumn, respectively. The remaining case is $L \sim \frac{1}{R_e}$, in which significant seasonal current speed variation does not occur.

Next, we estimate the difference between v_a values on the eastern and western sides of the jet based on the numerical model output. Here, the difference between the average current speed on

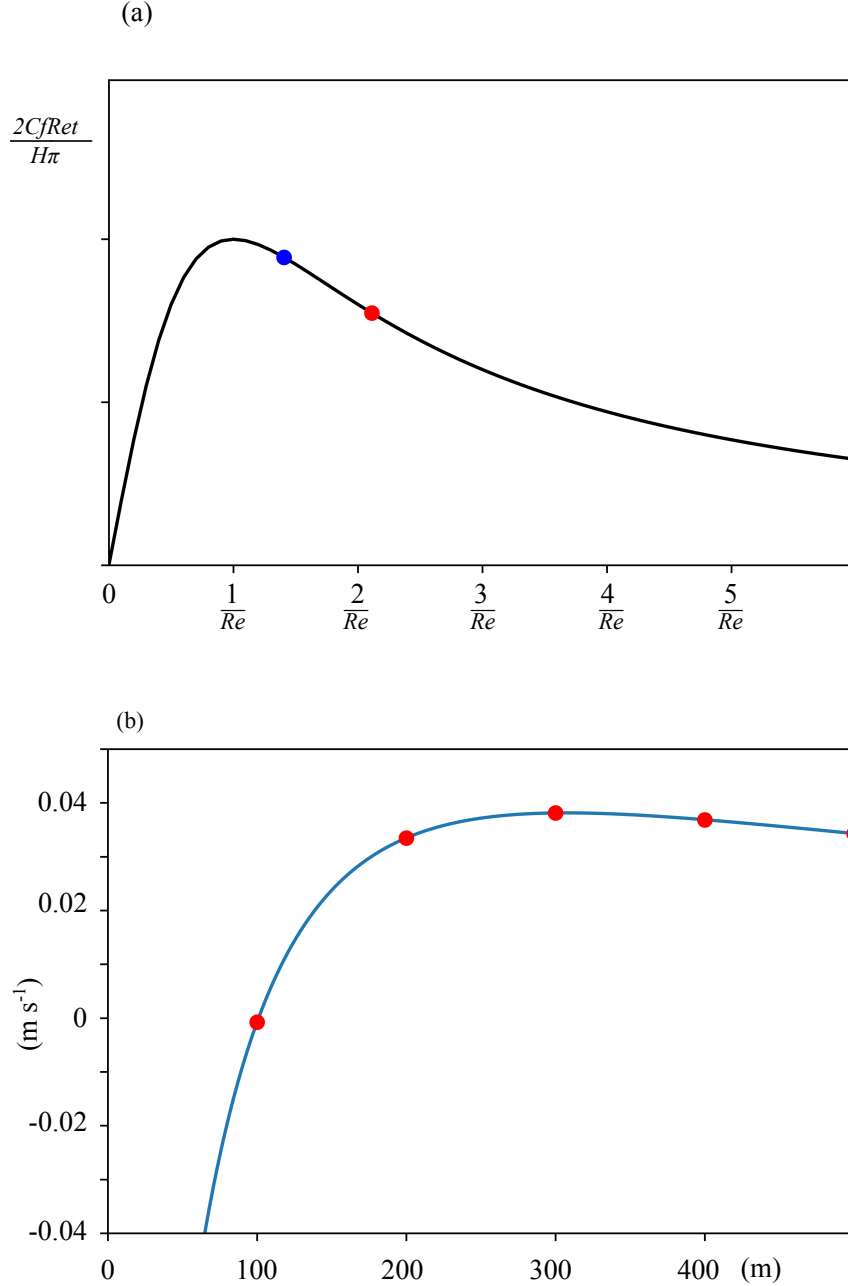


FIG. 24. (a) v_a as a function of k (Eq. (45)). (b) v_{ad} as a function of H (Eq. (46)). The following values are used: $k_W=6.28 \times 10^{-5} \text{ m}^{-1}$, $k_E=4.19 \times 10^{-5} \text{ m}^{-1}$, $g'=0.2 \text{ m s}^{-2}$, $f=7.29 \times 10^{-5}$, $C=2 \times 10^{-5} \text{ m s}^{-1}$ and $t=4.3 \times 10^6 \text{ s}$ (50 days). The red and blue dots in (a) indicate the values calculated by Eq. (45) using k_W and k_E , respectively.

the western and eastern sides of the jet (v_{ad}) is defined as:

$$v_{ad} = \frac{2Cft}{H\pi} \left(\frac{k_E}{k_E^2 + \frac{1}{R_e^2}} - \frac{k_W}{k_W^2 + \frac{1}{R_e^2}} \right) \quad (46)$$

To estimate k_W and k_E , the velocity profile from the numerical model output was curve-fitted using the function given by Eqs. (30-31) on each side of the jet (blue line in Figure 23). The resulting k_W and k_E are $6.28 \times 10^{-5} \text{ m}^{-1}$ and $4.19 \times 10^{-5} \text{ m}^{-1}$, respectively. Because v_{ad} varies with H and R_e depends on H , we investigate the dependency of v_{ad} on H . Assuming $g' = 0.02 \text{ m}^{-1}$, $f = 7.29 \times 10^{-5}$, $C = 2 \times 10^{-5} \text{ m s}^{-1}$ (derived from Figure 21) and $t \approx 3.5\text{--}4.3 \times 10^6 \text{ s}$ ($\sim 40\text{--}50 \text{ d}$), the current speed increases in summer and decreases in autumn for H larger than 100 m (Figure 24). The maximum value of v_{ad} is $\sim 0.03\text{--}0.04 \text{ m s}^{-1}$, at H of approximately 250 m. This value is $\sim 45\%\text{--}50\%$ of the near-surface current speed variation simulated by the numerical model ($0.067\text{--}0.08 \text{ m s}^{-1}$). The basic equations of the analytical model (Eqs. (9-11)) did not include nonlinear advection terms, and the velocity change in the present model was explained only by the local effect. Therefore, the basic equations used in this study are consistent with those from a model with an infinite model domain in the meridional direction. For a mode with a finite domain, the nonlinear advection effect may play an important role in explaining the current speed variation.

The Rossby deformation radius (R_e) is another parameter involved in the background jet state, including the horizontal distributions of g and H . The sensitivity of this parameter may be checked mathematically by solving Eq. (22), with an x -dependent R_e for $k > \frac{1}{R_e}$. However, the equation is difficult to solve, even when $R_e(x)$ is a linear function. Therefore, we tested the discontinuous solution given by Eq. (45), which is rearranged with respect to R_e as follows:

$$v_a = \frac{2}{\pi} \left(\frac{Cktg'}{R_e^2 k^2 f + f} \right) \quad (47)$$

Assuming that R_e is larger on the eastern side than on the western side, Eq. (47) implies that the horizontally averaged current speed (v_a) is smaller on the eastern side than on the western side for all domains of x . Therefore, R_e —unlike the wavelength—is not an explanatory factor.

5.3 Application of the hypothesis over the entire Kuroshio path

In this section, the application of the driving mechanism proposed in section 4 to other areas over the entire Kuroshio path is examined. According to the observational data analysis shown in Figure 14, the amplitude of the seasonal along-stream current speed variation and that of the along-stream 10-m wind speed variation on the Kuroshio are 0.1 and 7 m s⁻¹ averaged over the entire Kuroshio path, respectively. The results from the numerical model configured for the ECS in this study showed that the along-stream wind stress variation with an amplitude of 0.2 Pa produces a current speed variation of 0.08 m s⁻¹. Using a simple bulk formula with a drag coefficient of 1.2×10^{-3} , a wind stress of 0.2 Pa can be converted to a wind speed of 14 m s⁻¹, which is approximately twice as large as the result shown in Figure 14. Considering a linear response of the current speed to the wind stress variation (results not shown), the numerical mode explains approximately 30%–40% of the observed current speed variation averaged over the entire Kuroshio path. The average amplitude of the seasonal current speed variation is 0.05 m s⁻¹ in the ECS but increases to 0.1 m s⁻¹ over the entire Kuroshio path. Thus, the current speed variation has local differences that may be explained by different effects on current speed anomaly advection and asymmetrical jet profiles.

6. Summary

To obtain a unified view of the seasonal variation features over the entire Kuroshio path, a satellite altimetry dataset and a reanalysis dataset were analyzed in this study. For a better understanding of the differences between the seasonal variations in the upper layer and the lower layer, velocity variations were investigated at several depths in addition to calculating the volume transport. The

primary results obtained from the current data analysis are as follows: 1) the seasonal variations in the upper layer (0-500 m depth) differ from those in the lower layer (> 500 m depth). Within the upper layer, the seasonal velocity variation maximum appears primarily in July over the entire Kuroshio path, while the minimum occurs in autumn (October to November) and winter (January to February), depending on the region. 2) However, the seasonal velocity variation maximum in the lower layer appears in winter (December to February) over the broad area from the east of Luzon Island to the east of Kyushu through the region east of the Ryukyu Island chain, which is regarded as a route of the deeper Kuroshio flow. Independent of the region, the lower layer seasonal velocity variation minimum appears mostly during autumn (from September to November) over the whole region.

The essential dynamics of the seasonal velocity variations in different layers were clarified through numerical experiments using a regional model with a realistic bottom topography. Special attention was paid to the effect of wind stress over the WBR on seasonal surface velocity variations. The control experiment (Exp-1), which was driven by the annual-cycle wind stress variation over the whole model domain, reproduced the essential features of the seasonal velocity variations observed at different depths. Specifically, within the upper layer, the maximum of seasonal velocity variations appeared primarily in summer, whereas within the lower layer (> 500 m depth), the maximum appeared in winter. In Exp-2, in which the wind stress was removed over the entire WBR, the results clearly demonstrated that the seasonal velocity variation maximum in the upper layer was no longer found in July over the entire Kuroshio path but that such variations in the lower layer showed no significant differences from those in Exp-1. However, the seasonal velocity variations in Exp-2 suffered the influence of the artificial wind stress curl associated with the removal of the wind stress within the WBR, and thus, additional experiments were needed to clarify the impact of local wind stress on the seasonal velocity variations over the entire WBR. We, therefore, carried

out Exp-3 (no wind stress in the ECS) and Exp-4 (no wind stress near the north of Taiwan), in both of which the barotropic Rossby waves into the ECS, which were emitted by the artificial wind stress curl, were mostly blocked by the Ryukyu Island chain. The results of these experiments revealed that seasonal velocity variations in the upper layer in the ECS were primarily forced by local wind stress upon the Kuroshio and secondarily influenced by downstream advection. Considering that the seasonal surface velocity variations had a similar feature over the entire Kuroshio path, we inferred that the local wind stress was a primary driving force for not only the seasonal surface velocity variations in the ECS but also in the other Kuroshio regions.

These results indicate that the conventional mechanisms deemed responsible for seasonal Kuroshio transport variations were not responsible for the numerical results. More specifically, neither the flow-topography interactions nor the coastal upwelling/downwelling process are the essential mechanism for the Kuroshio upper-layer seasonal velocity variations. To clarify the dynamics of the seasonal velocity variation in the upper layer of the Kuroshio, a simple numerical model with idealized bottom topography and an a rigid-lid reduced-gravity model with Ekman layer dynamics were used to investigate the response of a jet to sudden winds. It turned out that the asymmetry of the horizontal velocity profile relative to the current axis position is a key factor underlying the current speed variation: with a higher wavenumber on the westside of the jet, the analytical model successfully reproduced that a current speed increases under summer wind condition and decreases under autumn wind condition. The asymmetry of the horizontal velocity profile with a smaller current width on the western side of the jet can also be found in the output from the OGCM of the Earth Simulator (referred to as OFES) (see Figure 14 in Nakamura et al. (2010)), and in the observational data for the Kuroshio southeast of Kyushu (see Figure 5 in Nakamura et al. (2012), although the jet's velocity profile showed a reversed tendency for some cases). Furthermore, the velocity profile of the Gulf Stream was observed to have the same

asymmetrical feature of a smaller current width on the western side (see Figure 2 in Rossby and Zhang (2001)). The reason for the asymmetric velocity profile of the jet was not examined in this study, and thus it should be clarified in future studies. Furthermore, the role of the nonlinear advection effect in the current speed variation was not examined in the analytical model, because the mode was configured with an infinite domain in the meridional direction. The investigation of the role of the nonlinear advection effect remains as an interesting future study. Finally, it addresses that the dynamics proposed in this study can underlies in not only the seasonal surface velocity variation of the Kuroshio in the ECS but also those variations over the entire Kuroshio path, which was regarded as a unified feature over the entire Kuroshio path in this study. In addition to the seasonal variations, it is also expected that the proposed dynamics could be applied to interannual and decadal variations in the upper layer of the Kuroshio through the modulation of the Northeast Asian Monsoon. Investigating the relationship between the interannual and decadal variations of the upper layer of the Kuroshio and the Northeast Asian Monsoon are considered as an interesting topic among future studies.

For the seasonal variations in the lower layer, the nontopographic Sverdrup response to seasonal wind stress curl in the interior region west of the Izu-Ogasawara Ridge was examined. Both the phase and amplitude predicted by the nontopographic Sverdrup theory were consistent with numerically simulated values, which were obtained by calculating the volume transport from 500 m depth to the bottom on the eastern slope of the Ryukyu Island chain. These features suggest that seasonal velocity variations in the lower layer are dominated by the barotropic response to wind stress curl over the area west of the Izu-Ogasawara Ridge. The reason why the winter maximum predicted by the Sverdrup theory was not clearly detected as part of the observed upper-layer seasonal velocity variations is that the seasonal velocity variations that result from the nontopographic Sverdrup responses are smaller in amplitude than the those of the upper layer

variations. However, if we consider the seasonal Kuroshio transport variations estimated for the water column from the sea surface to depths over 1000 m, we can detect a semiannual cycle with maxima in winter and summer for a combined feature of the two responses, as shown for the region south of Japan by Isobe and Imawaki (2002) and for the Tokara Strait by Zhu et al. (2017).

Acknowledgments. I express my best gratitude to my advisor, Professor Hirohiko Nakamura, who kindly supported my research and provided necessary conditions for my life in Japan. I also give my sincere thanks to Professor Ryuichiro Nishi and Assistant Professor Ayako Nishina for the helpful comments and suggestions during the years.

References

- Amante, C., and B. W. Eakins, 2009: Etopo1 1 arc-minute global relief model: Procedures, data sources and analysis. NOAA Technical Memorandum NESDIS NGDC-24. National Geophysical Data Center, NOAA, <https://doi.org/10.7289/V5C8276M>.
- Anderson, D., and R. Corry, 1985: Seasonal transport variations in the florida straits: A model study. *J. Phys. Oceanogr.*, **15** (6), 773–786, [https://doi.org/10.1175/1520-0485\(1985\)015<0773:STVITF>2.0.CO;2](https://doi.org/10.1175/1520-0485(1985)015<0773:STVITF>2.0.CO;2).
- Andres, M., M. Wimbush, J.-H. Park, K.-I. Chang, B.-H. Lim, D. R. Watts, H. Ichikawa, and W. J. Teague, 2008: Observations of kuroshio flow variations in the east china sea. *J. Geophys. Res.*, **113** (C5), <https://doi.org/10.1029/2007jc004200>.
- Blumberg, A., and G. Mellor, 1987: A description of a three-dimensional coastal ocean circulation model, three-dimensional coastal ocean models. *Coastal Estuarine Sci.*, **4**, 1–16, <https://doi.org/10.1029/co004p0001>.

- Chang, Y.-L., and L.-Y. Oey, 2011: Interannual and seasonal variations of kuroshio transport east of taiwan inferred from tide-gauge data. *Geophys. Res. Lett.*, **38** (8), <https://doi.org/10.1029/2011gl047062>.
- Conkright, M. E., R. A. Locarnini, H. E. Garcia, T. D. O'Brien, T. P. Boyer, C. Stephens, and J. I. Antonov, 2002: World ocean atlas 2001: Objective analyses, data statistics, and figures: Cd-rom documentation.
- Czeschel, L., C. Eden, and R. Greatbatch, 2012: On the driving mechanism of the annual cycle of the florida current transport. *J. Phys. Oceanogr.*, **42** (5), 824–839, <https://doi.org/10.1175/JPO-D-11-0109.1>.
- Gilson, J., and D. Roemmich, 2002: Mean and temporal variability in kuroshio geostrophic transport south of taiwan (1993–2001). *J. Oceanogr.*, **58** (1), 183–195, <https://doi.org/10.1023/A:1015841120927>.
- Greatbatch, R., and A. Goulding, 1989a: Seasonal variations in a linear barotropic model of the north atlantic driven by the hellerman and rosenstein wind stress field. *J. Phys. Oceanogr.*, **19** (5), 572–595, [https://doi.org/10.1175/1520-0485\(1989\)019<0572:SVIALB>2.0.CO;2](https://doi.org/10.1175/1520-0485(1989)019<0572:SVIALB>2.0.CO;2).
- Greatbatch, R., and A. Goulding, 1989b: Seasonal variations in a linear barotropic model of the north pacific driven by the hellerman and rosenstein wind stress field. *J. Geophys. Res.*, **94** (C9), 12 645–12 665, <https://doi.org/10.1029/jc094ic09p12645>.
- Greatbatch, R., and A. Goulding, 1990: On the seasonal variation of transport through the tokara strait. *J. Oceanogr. Soc. Japan*, **46**, 9–20, <https://doi.org/10.1007/BF02334220>.
- Guo, X., X.-H. Zhu, Q.-S. Wu, and D. Huang, 2012: The kuroshio nutrient stream and its temporal variation in the east china sea. *J. Geophys. Res. Oceans*, **117** (C1).

- Haney, R. L., 1971: Surface thermal boundary condition for ocean circulation models. *J. Phys. Oceanogr.*, **1** (4), 241–248, [https://doi.org/10.1175/1520-0485\(1971\)001<0241:STBCFO>2.0.CO;2](https://doi.org/10.1175/1520-0485(1971)001<0241:STBCFO>2.0.CO;2).
- Hsin, Y.-C., B. Qiu, T.-L. Chiang, and C.-R. Wu, 2013: Seasonal to interannual variations in the intensity and central position of the surface kuroshio east of taiwan: Variations of kuroshio east of taiwan. *J. Geophys. Res.*, **118**, 4305–4316, <https://doi.org/10.1002/jgrc.20323>.
- Ichikawa, H., and R. C. Beardsley, 1993: Temporal and spatial variability of volume transport of the kuroshio in the east china sea. *Deep-Sea Res. I*, **40**, 583–605, [https://doi.org/10.1016/0967-0637\(93\)90147-U](https://doi.org/10.1016/0967-0637(93)90147-U).
- Ichikawa, H., H. Nakamura, A. Nishina, and M. Higashi, 2004: Variability of northeastward current southeast of northern ryukyu islands. *J. Oceanogr.*, **60** (2), 351–363, <https://doi.org/10.1023/B:JOCE.0000038341.27622.73>.
- Imawaki, S., 1997: Time series of the kuroshio transport derived from field observations and altimetry data. *International WOCE Newsletter*, **25**, 15–18.
- Imawaki, S., H. Uchida, H. Ichikawa, M. Fukasawa, and S.-I. Umatani, 2001: Satellite altimeter monitoring the kuroshio transport south of japan. *Geophys. Res. Lett.*, **28** (1), 17–20, <https://doi.org/10.1029/2000gl011796>.
- Isobe, A., and S. Imawaki, 2002: Annual variation of the kuroshio transport in a two-layer numerical model with a ridge. *J. Phys. Oceanogr.*, **32** (3), 994–1009, [https://doi.org/10.1175/1520-0485\(2002\)032<0994:AVOTKT>2.0.CO;2](https://doi.org/10.1175/1520-0485(2002)032<0994:AVOTKT>2.0.CO;2).

- Johns, W., T. Lee, D. Zhang, R. Zantopp, C.-T. Liu, and Y. Yang, 2001: The kuroshio east of taiwan: Moored transport observations from the woce pcm-1 array. *J. Phys. Oceanogr.*, **31** (4), 1031–1053, [https://doi.org/10.1175/1520-0485\(2001\)031<1031:TKEOTM>2.0.CO;2](https://doi.org/10.1175/1520-0485(2001)031<1031:TKEOTM>2.0.CO;2).
- Kagimoto, T., and T. Yamagata, 1997: Seasonal transport variations of the kuroshio: An ogcm simulation. *J. Phys. Oceanogr.*, **27** (3), 403–418, [https://doi.org/10.1175/1520-0485\(1997\)027<0403:STVOTK>2.0.CO;2](https://doi.org/10.1175/1520-0485(1997)027<0403:STVOTK>2.0.CO;2).
- Kalnay, E., and Coauthors, 1996: The ncep/ncar 40-year reanalysis project. *Bull. Amer. Meteor. Soc.*, **77** (3), 437–472, [https://doi.org/10.1175/1520-0477\(1996\)077<0437:TNYRP>2.0.CO;2](https://doi.org/10.1175/1520-0477(1996)077<0437:TNYRP>2.0.CO;2).
- Kasai, A., K. Komatsu, C. Sassa, and Y. Konishi, 2008: Transport and survival processes of eggs and larvae of jack mackerel *trachurus japonicus* in the east china sea. *Fisheries Science*, **74** (1), 8–18.
- Kawabe, M., 1995: Variations of current path, velocity, and volume transport of the kuroshio in relation with the large meander. *J. Phys. Oceanogr.*, **25** (12), 3103–3117, [https://doi.org/10.1175/1520-0485\(1995\)025<3103:VOCPVA>2.0.CO;2](https://doi.org/10.1175/1520-0485(1995)025<3103:VOCPVA>2.0.CO;2).
- Kubota, M., H. Yokota, and T. Okamoto, 1995: Mechanism of the seasonal transport variation through the tokara strait. *J. Oceanogr.*, **51** (4), 441–458, <https://doi.org/10.1007/BF02286391>.
- Masumoto, Y., and Coauthors, 2004: A fifty-year eddy-resolving simulation of the world ocean: Preliminary outcomes of OFES (OGCM for the earth simulator). *J. Earth Simulator*, **1**, 35–56.
- Mellor, G., L.-Y. Oey, and T. Ezer, 1998: Sigma coordinate pressure gradient errors and the seamount problem. *J. Atmos. Oceanic Tech.*, **15** (5), 1122–1131, [https://doi.org/10.1175/1520-0426\(1998\)015<1122:SCPGEA>2.0.CO;2](https://doi.org/10.1175/1520-0426(1998)015<1122:SCPGEA>2.0.CO;2).

- Nakamura, H., R. Hiranaka, D. Ambe, and T. Saito, 2015: Local wind effect on the kuroshio path state off the southeastern coast of kyushu. *J. Oceanogr.*, **71 (5)**, 575–596, <https://doi.org/10.1007/s10872-015-0309-1>.
- Nakamura, H., H. Ichikawa, and A. Nishina, 2007: Numerical study of the dynamics of the ryukyu current system. *J. Geophys. Res.*, **112 (C4)**, <https://doi.org/10.1029/2006jc003595>.
- Nakamura, H., A. Nishina, K. Tabata, M. Higashi, A. Habano, and T. Yamashiro, 2012: Surface velocity time series derived from satellite altimetry data in a section across the kuroshio southwest of kyushu. *J. Oceanogr.*, **68 (2)**, 321–336.
- Nakamura, H., M. Nonaka, and H. Sasaki, 2010: Seasonality of the kuroshio path destabilization phenomenon in the okinawa trough: a numerical study of its mechanism. *J. Phys. Oceanogr.*, **40 (3)**, 530–550.
- Niiler, P. P., 1969: On the ekman divergence in an oceanic jet. *J. Geophys. Res.*, **74 (28)**, 7048–7052, <https://doi.org/10.1029/jc074i028p07048>.
- Rosby, T., and H.-M. Zhang, 2001: The near-surface velocity and potential vorticity structure of the gulf stream. *J. Mar. Res.*, **59 (6)**, 949–975.
- Sakamoto, T., and T. Yamagata, 1996: Seasonal transport variations of the wind-driven ocean circulation in a two-layer planetary geostrophic model with a continental slope. *J. Mar. Res.*, **54 (2)**, 261–284, <https://doi.org/10.1357/0022240963213402>.
- Sasaki, H., and Coauthors, 2004: A series of eddy-resolving ocean simulations in the world ocean: OFES (OGCM for the earth simulator) project. *OCEAN'04*, **3**, 1535–1541.

- Schott, F., T. Lee, and R. Zantopp, 1988: Variability of structure and transport of the florida current in the period range of days to seasonal. *J. Phys. Oceanogr.*, **18** (9), 1209–1230, [https://doi.org/10.1175/1520-0485\(1988\)018<1209:VOSATO>2.0.CO;2](https://doi.org/10.1175/1520-0485(1988)018<1209:VOSATO>2.0.CO;2).
- Sekine, Y., and K. Kutsuwada, 1994: Seasonal variation in volume transport of the kuroshio south of japan. *J. Phys. Oceanogr.*, **24** (2), 261–272, [https://doi.org/10.1175/1520-0485\(1994\)024<0261:SVIVTO>2.0.CO;2](https://doi.org/10.1175/1520-0485(1994)024<0261:SVIVTO>2.0.CO;2).
- Sheremet, V. A., 2001: Hysteresis of a western boundary current leaping across a gap. *J. Phys. Oceanogr.*, **31** (5), 1247–1259, [https://doi.org/10.1175/1520-0485\(2001\)031<1247:HOAWBC>2.0.CO;2](https://doi.org/10.1175/1520-0485(2001)031<1247:HOAWBC>2.0.CO;2).
- Thoppil, P., E. Metzger, H. Hurlburt, O. Smedstad, and H. Ichikawa, 2016: The current system east of the ryukyu islands as revealed by a global ocean reanalysis. *Prog. Oceanogr.*, **141**, 239–258, <https://doi.org/10.1016/j.pocean.2015.12.013>.
- Tian, J., Q. Yang, X. Liang, L. Xie, D. Hu, F. Wang, and T. Qu, 2006: Observation of luzon strait transport. *Geophys. Res. Lett.*, **33** (19), <https://agupubs.onlinelibrary.wiley.com/doi/abs/10.1029/2006GL026272>.
- Usui, N., H. Tsujino, H. Nakano, and S. Matsumoto, 2013: Long-term variability of the kuroshio path south of japan. *J. Oceanogr.*, **69** (6), 647–670, <https://doi.org/10.1007/s10872-013-0197-1>.
- Wu, C.-R., and Y.-C. Hsin, 2012: The forcing mechanism leading to the kuroshio intrusion into the south china sea. *J. Geophys. Res. Oceans*, **117** (C7), <https://doi.org/10.1029/2012jc007968>.
- Xue, H., and G. Mellor, 1993: Instability of the gulf stream front in the south atlantic bight. *J. Phys. Oceanogr.*, **23** (11), 2326–2350.

- Yaremchuk, M., and T. Qu, 2004: Seasonal variability of the large-scale currents near the coast of the philippines. *J. Phys. Oceanogr.*, **34** (4), 844–855, [https://doi.org/10.1175/1520-0485\(2004\)034<0844:SVOTLC>2.0.CO;2](https://doi.org/10.1175/1520-0485(2004)034<0844:SVOTLC>2.0.CO;2).
- Zhu, X.-H., H. Nakamura, D. Menghong, A. Nishina, and T. Yamashiro, 2017: Tidal currents and kuroshio transport variations in the tokara strait estimated from ferryboat adcp data: Tidal currents and kuroshio transport in the tokara strait. *J. Geophys. Res. Oceans*, **122** (3), 2120–2142, <https://doi.org/10.1002/2016jc012329>.
- Zhu, X.-H., and Coauthors, 2003: The northeastward current southeast of okinawa island observed during november 2000 to august 2001. *Geophys. Res. Lett.*, **30** (2), <https://doi.org/10.1029/2002gl015867>.